Analysis of the momentum recovery in the wake of aligned axial-flow hydrokinetic turbines

A. Posa and R. Broglia

View Online   Export Citation   CrossMark

ARTICLES YOU MAY BE INTERESTED IN

Dependence of tip and hub vortices shed by a propeller with winglets on its load conditions
Physics of Fluids **34**, 105107 (2022); https://doi.org/10.1063/5.0113480

Numerical investigation of a propeller operating under different inflow conditions
Physics of Fluids **34**, 105118 (2022); https://doi.org/10.1063/5.0109801

Supercritical flow characteristics in smooth open channels with different aspect ratios
Physics of Fluids **32**, 105102 (2020); https://doi.org/10.1063/5.0021609

AIP Publishing

Analysis of the momentum recovery in the wake of aligned axial-flow hydrokinetic turbines

View Online   Export Citation   CrossMark

A. Posa[a] (iD) and R. Broglia (iD)

AFFILIATIONS

CNR-INM, Institute of Marine Engineering, National Research Council of Italy, Via di Vallerano 139, 00128 Roma, Italy

[a]Author to whom correspondence should be addressed: antonio.posa@inm.cnr.it

ABSTRACT

Large-Eddy Simulations are reported, dealing with an axial-flow hydrokinetic turbine operating in the wake of an upstream one. Computations were conducted on a cylindrical grid consisting of 3.8×10^9 points, using an Immersed-Boundary methodology. The performance of the downstream turbine was negatively affected by the wake of the upstream one and substantially dependent on its distance. Results demonstrated a faster wake development, compared to the case of the same turbine operating in isolated conditions within a uniform flow, due to the faster instability of the tip vortices, induced by the perturbation of the inflow conditions by the wake of the upstream turbine. In contrast with the turbine performance, the process of wake recovery was found rather insensitive to the distance from the upstream turbine. In comparison with the case of the isolated turbine, the role of radial turbulent transport just downstream of the instability of the tip vortices was found especially important in accelerating the process of wake recovery at the outer radii, providing a significant contribution together with radial advection. Further downstream, the contribution by turbulent transport was verified reinforced also within the wake core, where instead momentum replenishment by radial advection was rather limited.

Published under an exclusive license by AIP Publishing. https://doi.org/10.1063/5.0117882

I. INTRODUCTION

Over the last few decades, the growing energy demand has been coupled with the increasing need of sustainable development, pushing toward renewable energy resources and improvements on the technology for their efficient exploitation (for a review of the state-of-the-art, see Hussain *et al.*[1]). In this framework, the kinetic energy of rivers, tides, and ocean currents has the potential of providing a significant contribution.[2] Research and technology in this field are less developed if compared, for instance, to those for wind energy. However, they actually share important similarities. Several devices utilized for the harvesting of hydrokinetic energy, as axial-flow and cross-flow turbines, were, indeed, developed from the existing technologies utilized by the wind energy industry. The potential of hydrokinetic energy is significant and will be certainly useful to complement more traditional energy resources for a cleaner and more sustainable development of the world economy.[3–5]

Hydrokinetic energy is a good candidate for increasing the share of power production from renewable energy resources, but more work needs to be done for its exploitation at large scale.[6] In particular, as in the field of wind energy, a major issue is represented by the mutual interaction of turbines deployed at the same site.[7,8] In general, this interaction is detrimental to the performance of downstream rows of turbines, decreasing the overall efficiency of the array. In addition, the coherent structures shed by upstream turbines produce unsteady loads on the downstream ones. It becomes necessary to properly design the relative position of the turbines composing the farm, in order to achieve larger levels of power production and lower fatigue loads, but avoiding too large distances between devices within the array (see, for instance, the experimental studies by Nuernberg and Tao,[9] Gaurier *et al.*,[10] and Okulov *et al.*[11,12]). Larger distances are, indeed, beneficial to the efficiency of each turbine, but increase the overall size of the array, resulting in larger costs of investment and in a more significant environmental impact of the installation.

The development of low-order models for the prediction of the wake signature of a hydrokinetic turbine is currently and in the near future mandatory to optimize or at least to improve the design of arrays, making hydrokinetic energy harvesting more convenient, decreasing its impact on the life of rivers and oceans, and promoting its large-scale exploitation. Performing accurate geometry-resolving simulations of several devices is not feasible now and in the foreseeable future, even on the most powerful supercomputers available in the world. For these reasons, simplified models are currently under development to be implemented into existing fluid dynamic solvers.

They utilize actuator disks or actuator lines, mimicking the action of the turbines on the flow, without explicitly resolving their geometry.[13–21] In other cases, analytical models of the wake of hydrokinetic turbines are developed, with the purpose of easing even more the overall computational burden.[22,23] Blade-element momentum models are also adopted, as in Pyakurel et al.,[24] Brunetti, Armenio, and Roman,[25] and Gotelli et al.[26] All these techniques were recently compared in terms of their suitability to reproduce the wake of an axial-flow turbine by Sandoval et al.[27] However, even more simplified approaches are utilized when dealing with large-scale simulations of arrays composed of several devices. For instance, Deng et al.[28] represented the momentum loss, associated with energy extraction by the turbines, by means of a momentum sink term added into the two-dimensional Navier–Stokes equations. In other cases, the action of the turbine on the current is mimicked introducing an additional bottom friction, as in the work by Zhang et al.[29]

Using reduced-order models of hydrokinetic turbines, as actuator disks or actuator lines, is especially useful for the simulation and the optimization of array configurations, due to limitations of the available computational resources.[30–40] Nonetheless, experiments and high-fidelity simulations of simplified configurations of interacting turbines are still required to develop an improved insight on the physics of the interaction and properly inform the community for a better design and validation of reduced-order approaches. For instance, the experimental studies conducted by Mycek et al.[41,42] and Gaurier et al.[10] were focused on the influence by the environmental turbulence on the wake interaction between upstream and downstream turbines. They verified that the drop in performance for the downstream turbine was a decreasing function of both streamwise distance and free-stream turbulence. Experiments on several layouts of axial-flow turbines were also conducted by Olczak et al.[43] to validate the performance of a blade-element model implemented within a Reynolds-averaged Navier–Stokes (RANS) solver. Larger modeling errors were found for those turbines whose inflow conditions were more affected by the wake of upstream devices. An array of four turbines was investigated by Nuernberg and Tao,[9] mimicking a modular unit of a staggered farm. Their study confirmed the potential of the layout of making available higher levels of momentum to downstream turbines by properly devising the lateral distance between devices, beneficially exploiting the blockage effects generated by the upstream staggered rows. Recently, Okulov et al.[12] studied an array composed of up to four in-line axial-flow hydrokinetic turbines. Interestingly, they verified that, while the second turbine experienced a significant drop in performance, which was consistent with earlier studies available in the literature, those more downstream performed better than the former.

A very small number of blade-resolving simulations of in-line turbines or simplified arrays is available in the literature. Liu et al.[44] utilized RANS to investigate the mutual interaction of in-line axial-flow turbines, placed at a distance of 8 diameters between each other, using a sliding mesh technique to take into account the rotation of the blades of the turbines and using a number of grid cells of the order $O(10^7)$. They verified that the downstream turbine experienced a drop in performance of more than 50% and increased lateral loads, while the upstream one was practically unaffected. Nuernberg and Tao[45] reported RANS computations on a modular array of turbines analyzed experimentally in their earlier work[9] and using an overall number of grid points up to 3 million. The lateral spacing of the turbines in a staggered layout was varied to assess its influence on the rate of wake

recovery, with the purpose of improving the working conditions of the most downstream turbine.

In the present work, a significant step forward is reported in the high-fidelity simulation of the interaction between two in-line axial-flow hydrokinetic turbines. Large-Eddy Simulations (LES) were conducted on a cylindrical grid consisting of almost 4×10^9 points, using an Immersed-Boundary (IB) methodology to handle the motion of the turbines. LES, resolving accurately the dynamics of all large, coherent structures populating the wake flow, is especially well suited to tackle the present problem and reproduce the physics of wake recovery. Earlier works have, indeed, demonstrated that the instability of the tip vortices shed from the blades of the turbines defines the boundary between the near wake and the region of wake recovery,[46–52] where both inward radial flows and turbulent transport allow the free-stream momentum to penetrate into the wake core, making available more kinetic energy at the inflow of downstream turbines. In particular, this study is an extension of our earlier work.[53] We utilized the data from high-fidelity simulations of the wake flow to analyze in detail the different terms of the momentum balance equation. This analysis was correlated with the flow physics and, in particular, with the instability of the tip vortices at the outer boundary of the wake. As long as they keep stable, they delay the process of wake recovery downstream of the rotor. All terms contributing to the momentum balance are analyzed across three configurations of two in-line turbines, differing for the distance between them. Comparisons are also presented against the results from the simulation of the same turbine in isolated conditions and uniform flow. The analysis will demonstrate that the process of wake recovery, beginning at the breakup of the tip vortices, is dominated by radial advection and especially by turbulent transport, which is very important to complete the momentum replenishment at inner radii. This process will be shown to be weakly sensitive to the distance from the upstream turbine, albeit in all cases much faster than in the wake of an isolated turbine. This analysis provides new insights on the physics of the process of wake recovery of a turbine operating in the wake of an upstream one, on the influence of their mutual distance on this process, and is expected to serve as a reference for checking and tuning the behavior of reduced-order models, often utilized to represent the wake development of axial-flow turbines for the simulation of large arrays. For instance, RANS techniques can be expected to capture properly the initial stage of recovery associated with the mean radial gradients and the instability of the large tip vortices. In contrast, the turbulent transport tied to the small scales, produced by the breakup of the tip vortices, needs to be modeled. It is not straightforward that turbulence modeling is able to mimic accurately the latter physics.

This paper is organized as follows: methodology in Sec. II, design of the simulations in Sec. III, analysis of the result in Sec. IV, and conclusions in Sec. V.

II. METHODOLOGY

The filtered Navier–Stokes equations for incompressible flows were resolved. Their expression in non-dimensional form is below:

$$D(\widetilde{\boldsymbol{u}}) = 0, \tag{1}$$

$$\frac{\partial \widetilde{\boldsymbol{u}}}{\partial t} + D(\widetilde{\boldsymbol{u}}\widetilde{\boldsymbol{u}}) = -G(\widetilde{p}) - D(\boldsymbol{\tau}) + \frac{1}{Re}L(\widetilde{\boldsymbol{u}}) + \boldsymbol{f}, \tag{2}$$

where Eq. (1) enforces the conservation of mass and Eq. (2) the conservation of momentum. The symbols D, G, and L represent the

divergence, gradient, and Laplace operators. The quantities $\widetilde{u}$ and $\widetilde{p}$ are the filtered velocity vector and pressure and t is the time variable. Re is the Reynolds number, defined as $Re = UL/\nu$, where U is a reference velocity, L is a reference length, and ν is the kinematic viscosity of the fluid. In the present work, the reference velocity and length, utilized to scale the Navier–Stokes equations, were selected as $U = U_\infty$ and $L = D$, where U_∞ is the free-stream velocity and D is the rotor diameter of the turbine.

The quantity τ is the subgrid stress (SGS) tensor. It is an additional term, compared to the original Navier–Stokes equations, coming from filtering them: $\tau = \widetilde{uu} - \widetilde{u}\widetilde{u}$. Practically, the size of the filter is defined by the resolution of the adopted computational grid, which is, in general, unable to resolve all scales of the flow, up to the smallest one (Kolmogorov's scale). Therefore, the SGS tensor mimics the action of the smallest, unresolved scales on the largest, resolved ones. In this study, its parameterization was based on an eddy-viscosity assumption, as typical in LES, using the Wall-Adapting Local Eddy-viscosity (WALE) model, developed by Nicoud and Ducros.[54] It is based on the square of the gradient tensor of the resolved velocity field. This way it is able to include both its deformation and rotation tensors, switching-off in areas of laminar gradients. In addition, the eddy-viscosity is reconstructed in order to achieve the correct near wall behavior, that is its dependence on the cube distance from the wall. Since this is a local eddy-viscosity model and does not require *ad hoc* reconstructions in the near wall regions, its computational overhead is equivalent to only a few percent of the overall computational cost. The WALE model was already successfully utilized to simulate the same isolated turbine by Posa and Broglia.[51,52] In particular, Posa and Broglia[51] demonstrated its ability of reproducing the strong anisotropy of turbulence in the wake.

The quantity f within the momentum equation is a forcing term, utilized in this study to enforce the no-slip boundary condition on the surface of the turbine, via an IB methodology. This relaxes the requirement for the Eulerian grid, where the Navier–Stokes equations are resolved, to fit the geometry of the body immersed within the flow. This is instead represented by means of a suitable Lagrangian grid, free to move across the cells of the Eulerian grid. These features of the IB methodology enable using regular Eulerian grids, with beneficial effects on the accuracy of eddy-resolving simulations. In addition, the Lagrangian grid is allowed to move within the Eulerian grid, making very straightforward handling flow problems featuring moving bodies. In the present computations, the quantity f was defined to enforce at all points of the Eulerian grid falling inside the volume of the immersed-boundary, bounded by the surface approximated by the Lagrangian grid, a velocity boundary condition corresponding to the velocity of the body. For the points of the Eulerian grid placed outside of the body, but in the vicinity of at least one interior node, which are the interface nodes, a linear reconstruction of the solution along the normal to the surface of the Lagrangian grid was enforced, again by means of f. This was defined in such a way to have the relative velocity on the surface of the body equal to 0. A detailed discussion on the IB methodology and its particular implementation within the adopted solver is not within the scope of the present work, but more information can be found in Balaras,[55] Yang and Balaras,[56] and Yang et al.[57] This is the same technique utilized to simulate the isolated turbine by Posa and Broglia[51,52] and Posa et al.[58] Similar applications in the fields of marine propulsion and wind energy can be found in recent works.[59–65]

The numerical solution of the filtered Navier–Stokes equations was achieved by discretization in space, using second-order, central finite differences on a staggered cylindrical grid. As demonstrated by Fukagata and Kasagi,[66] this strategy satisfies the conservation of mass, momentum, and kinetic energy by the discretized version of the flow problem, which is a critical requirement for the accuracy of eddy-resolving computations. The advancement in time was conducted using an exact projection method.[67] In particular, the discretization in time of all viscous, convective, and SGS terms of radial and axial derivatives utilized the explicit three-step Runge–Kutta (RK3) scheme. For all terms of azimuthal derivatives within the momentum equation the implicit Crank–Nicolson (CN) scheme was instead adopted, to avoid unaffordable requirements on the size of the time step, coming from the decreasing size of the grid cells toward the axis of the cylindrical grid. For the solution of the Poisson problem, stemming from the continuity condition, trigonometric transformations were utilized across the periodic azimuthal direction, decomposing its original heptadiagonal system of equations into a pentadiagonal system for each meridian slice of the cylindrical grid. Each of them was efficiently inverted by using a direct solver, based on the partial solution variant of the cyclic reduction algorithm, developed by Rossi and Toivanen.[68] The overall Navier–Stokes solver was demonstrated second-order accurate in both space and time by Balaras[55] and Yang and Balaras,[56] where additional details can be found.

III. SETUP

In this study, the rotor of a three-bladed, axial-flow hydrokinetic turbine is considered, whose simulation in isolated conditions and uniform flow was analyzed in our earlier works.[51,52,58] This configuration will be indicated in the following discussion as *IST*. The choice of simulating this configuration in conditions of no free-stream turbulence was tied to the need of reproducing similar working conditions as in the experimental "Round Robin" campaign by Gaurier et al.[69] They performed measurements in two towing tanks in the absence of free-stream turbulence and in two flume tanks at the lowest levels of turbulence intensity allowed by the facilities, equal to 2.5% and 3.0%, respectively. In the present work, the operation of the same turbine in the wake of an upstream one is studied for the same values of Tip Speed Ratio, $TSR = 5$, and Reynolds number, $Re = 560\,000$. This couple of values was selected to match one of the working conditions studied by Gaurier et al.[69] The former quantity is defined as $TSR = \Omega R/U_\infty$, where Ω is the angular speed of the turbine, R its radius, and U_∞ is the free-stream velocity. As discussed in Sec. II, the Reynolds number is based on the diameter of the turbine, D, and the free-stream velocity, U_∞: $Re = DU_\infty/\nu$. It should be acknowledged that free-surface effects were not accounted for by the simulations. This choice is in line with the reference experimental study.[69] They conducted measurements in both flume tanks, without free-surface, and in towing tanks, where the turbine model was immersed deep enough to make the free-surface effects negligible.

The present simulations considered the same blade geometry as Gaurier et al.[69] However, to ease the computational effort, the supporting stanchion utilized for the experiments was not included in the simulations, while a simplified hub geometry was modeled, as shown in Fig. 1. Its radius was equivalent to about 13% of the rotor radius, which is the same as for the actual model utilized in the experiments. The turbine considered by Gaurier et al.[69] had a diameter of 0.7 (m)
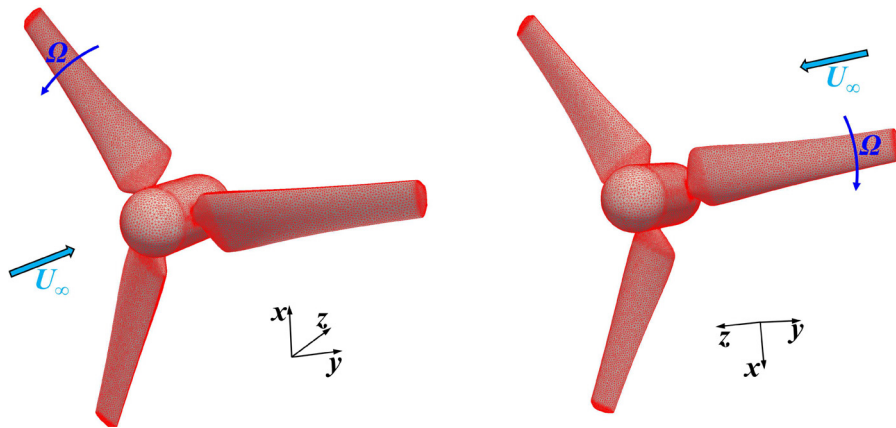
FIG. 1. Lagrangian grid discretizing the surface of the turbine: global views from upstream (left) and from downstream (right).

and its blades were designed using a NACA (National Advisory Committee for Aeronautics) 63-418 profile. Therefore, the case studied by Gaurier *et al.*[69] is a small-scale turbine, operating within a free-stream velocity between 0.6 and 1.2 (m/s). In particular, the present simulations assumed a free-stream velocity equal to 0.8 (m/s).

The inflow boundary conditions were defined using the database generated by our earlier computations in isolated conditions. From them, slices of the instantaneous solutions at 3 diameters downstream of the isolated turbine, representing in this study the upstream turbine, were stored. Then, they were adopted to generate inflow conditions for the simulations of the downstream turbines, by interpolating in time the instantaneous realizations of the solution within the database from the earlier computations. The exploitation of a precursor simulation to generate unsteady inflow boundary conditions suitable to LES is not new and was successfully utilized in several studies.[70–73] The accuracy of this approach relies on the optimal conservation properties of the solver, where the discretized version of the Navier–Stokes equations conserves mass, momentum, and kinetic energy. As a result, the inflow turbulence from the precursor simulation was sustained without the introduction of artificial source terms. In addition, the resolution of the computational grid was kept constant between the inflow section and the plane of the turbine, to avoid diffusion due to grid coarsening.

The enforced inflow conditions resulted into values of turbulence intensity ingested by the downstream turbines between 26% and 32%. They are higher than the free-stream turbulence measured in typical sites of installation of hydrokinetic turbines, reported for instance in the works by Mycek *et al.*[74] and Gaurier *et al.*[10] They pointed out that actual turbulence intensities can range from a few percent to values of more than 20%, showing a dramatic dependence on the site of the installation. However, our simulations demonstrated that the levels of turbulence caused by upstream devices are higher, making the intensity of free-stream turbulence a less important parameter in defining the working conditions of downstream devices. This is also in agreement with the results reported on in-line turbines by Mycek *et al.*,[42,74] where the wake development of the downstream turbine was found a much weaker function of the environmental turbulence, if compared with that of the upstream turbine.

Three cases were simulated, with the downstream turbine in line with the upstream one and placed at 6, 8, and 10 diameters away,

respectively. These cases will be designated in the following as *DT*6, *DT*8, and *DT*10, respectively. Therefore, the simulations of the downstream turbines were conducted using cylindrical grids having a streamwise extent between the inlet section of the computational domain and the rotor plane equal to 3, 5, and 7 diameters, taking into account that the inflow boundary conditions were generated using slices extracted from the simulations by Posa and Broglia[51,52] at three diameters downstream of the isolated turbine. This approach, which allowed us a substantial saving of computational resources, was assumed accurate enough: we verified in all simulations that the blockage generated on the flow by the rotor becomes significant only at about 1 diameter upstream of it. Therefore, even for the case *DT*6, at three diameters away from the upstream turbine its wake can still be assumed almost unaffected by the presence of another turbine placed six diameters downstream. The extent of the computational domain from the rotor plane to the outlet section as well as its radial size were kept unchanged, compared to those for the isolated turbine. Those lengths were equal to 7 and 6 diameters, respectively. The same conditions were also enforced at the outflow and lateral cylindrical boundaries of the domain, where convective and slip-wall conditions were prescribed, respectively. It should be noted, for the correct interpretation of the following discussion of the results, that the origin of the reference frame was placed at the intersection between the rotor plane and the axis of the cylindrical grid, which is also the axis of the turbine. The z axis was oriented in the direction of the free-stream. So the z coordinates define the distance from the rotor plane.

As in Posa and Broglia,[51,52] a structured cylindrical grid was utilized. However, the number of points was doubled across the axial direction, resulting in an overall number of 3.8×10^9: $900 \times 1026 \times 4098$ across the radial, azimuthal, and axial directions, respectively. Meridian slices of the cylindrical grids are shown in Fig. 2. It is worth noting that both in the left panels (overall slice) and in the right panels (detail in the vicinity of the turbine), only a few grid lines are shown, for clarity. Posa and Broglia[51,52] validated the results for the isolated turbine against the experiments reported by Gaurier *et al.*[69] Therefore, the grid resolutions across the radial and azimuthal directions were kept unchanged as well as that across the axial direction between the rotor plane and the outlet section of the computational domain. The axial resolution was instead substantially refined between the inlet section and the rotor plane, with the purpose of sustaining the inflow
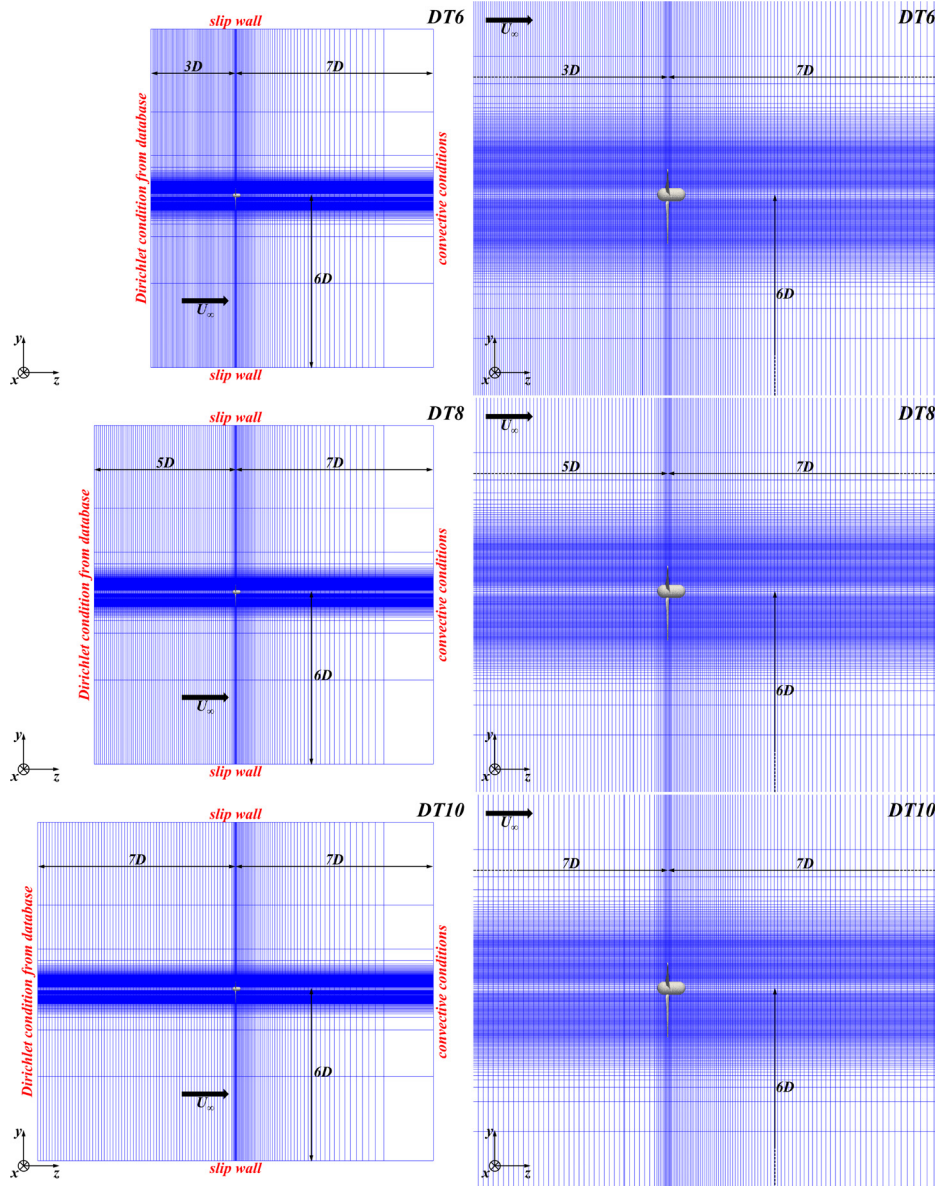
FIG. 2. Meridian slices of the cylindrical grids: global view on the left (1 of every 128 grid lines shown) and detail in the vicinity of the turbine on the right (1 of every 32 grid lines shown). Cases **DT6**, **DT8**, and **DT10** in the top, middle, and bottom panels, respectively.

turbulence coming from the upstream turbine. To achieve this target, the computational grids adopted for the three simulations of the downstream turbines were generated with the requirement to be, between the inlet section and the rotor plane, at least as fine as the one utilized for the simulations of the isolated turbine at $z/D = 3.0$, where the inflow boundary conditions for the present computations were extracted. Eventually, all three grids were designed to be even finer than the original one since all simulations were carried out in a High-Performance Computing environment: the requirements associated with parallel computing and decomposition into subdomains of the overall problem made convenient doubling the number of points across the streamwise direction in all cases, which was actually beneficial for both accuracy of the solution and efficiency of the solver.

Across the radial direction, about 600 points were distributed along the radius of the turbine, then the grid was smoothly stretched up to $r/D = 0.8$, to take into account the expansion of the wake downstream of the rotor plane and properly capture the behavior of the tip vortices. A uniform grid spacing was utilized across the azimuthal direction. It should be noted that, thanks to the IB methodology, simulations were conducted within a stationary Eulerian grid, rotating in time the Lagrangian grid representing the turbine. Therefore, the choice of a uniform azimuthal spacing was the most straightforward one. Across the axial direction, the three adopted grids were uniform between the inlet section and the region just upstream of the turbine. A finer uniform spacing was adopted within the region of the blades of the turbine. Then, smooth stretching was utilized
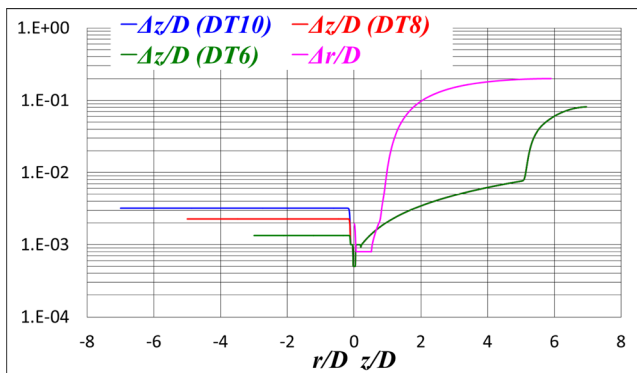
FIG. 3. Radial and axial spacings of the cylindrical grids. Note that the radial resolution is shared across cases *DT*6, *DT*8, and *DT*10.

downstream, up to $z/D = 5.0$. Stretching was eventually increased between $5.0 < z/D < 7.0$, up to the outlet section of the computational domain. Details on the radial and axial evolution of the grid spacing are reported in Fig. 3. As discussed above, all present grids feature an axial spacing in the upstream region $\Delta z/D < 4.8 \times 10^{-3}$, where the right-hand side (RHS) is the streamwise resolution of the grid adopted to generate the database of inflow boundary conditions. All cases share the same radial grid.

The discretization of the surface of the immersed-boundary, in this case the turbine, was achieved using an unstructured grid composed of about 75 000 triangular elements. It should be noted that this is the same one utilized for the earlier simulations of the isolated turbine within a uniform flow. A global view of both turbine geometry and its triangolarization is reported in Fig. 1, while details of the
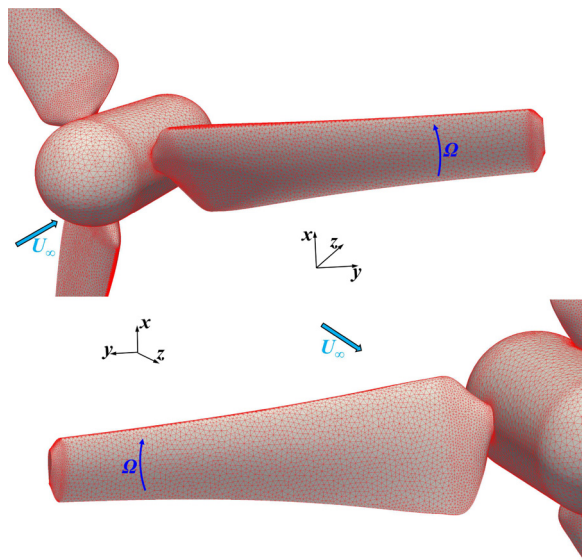

FIG. 4. Lagrangian grid discretizing the surface of the turbine: details of the blades from upstream (top) and from downstream (bottom).

pressure and suction sides of the blades are shown in the top and bottom panels of Fig. 4, respectively.

The resolution in time of all computations was defined by the stability requirements of the explicit RK3 scheme. Enforcing a value of the Courant–Friedrichs–Lewy (CFL) number equal to 1 resulted in an average time step $\Delta t = 1.56 \times 10^{-4} D/U_\infty$, equivalent to a rotation per time step equal to $0.089°$. This means that about four steps in time were required for the turbine to cross each cell of the computational grid along the azimuthal direction. All simulations were developed for two flow-through times before starting statistical sampling. This period of time, $\mathcal{T}$, was different across cases, due to the variable streamwise extent of the computational domain of the three simulations: it was $\mathcal{T} = 20D/U_\infty$, $\mathcal{T} = 24D/U_\infty$, and $\mathcal{T} = 28D/U_\infty$ for the cases *DT*6, *DT*8, and *DT*10, respectively, equivalent to about 32, 38, and 44 rotations. Then, after the development of the wake of the downstream turbines, statistical sampling was carried out during ten rotations for each case.

All simulations were performed by parallel computing, decomposing the cylindrical grids across the axial direction and using 2048 cores of a distributed-memory cluster, resulting in an overall computational cost equal to 2.1, 1.8, and 1.4 million core-hours for the cases *DT*10, *DT*8, and *DT*6, respectively.

IV. RESULTS

A. Definition of the time-average operators

Before discussing the results of the computations, some definitions of the time-average operators utilized for their statistical analysis will be reported. It should be noted that in the following, all discussions will refer to resolved quantities from LES results. Therefore, for the sake of simplicity, the symbol ∼ utilized in Sec. II to indicate filtered quantities will be dropped.

Averages in time were computed both as ensemble-averages and phase-averages. The former were computed on a stationary grid, whereas the latter on a grid rotating together with the turbine at the angular speed Ω, in order to capture the coherence of the vortices shed from the tip of its blades and the statistics within their core.

Considered any quantity, $\mathcal{Q}$, its ensemble-average was evaluated as

$$\bar{\mathcal{Q}}(r, z) = \frac{1}{\mathbb{M}} \sum_{i=1}^{\mathbb{M}} \mathcal{Q}(r, \vartheta, z, t_i), \tag{3}$$

where r, ϑ, and z are the radial, azimuthal, and axial coordinates within the cylindrical frame of reference, while t_i is the instant in time corresponding to the i-th element of the statistical sample, whose size was indicated by $\mathbb{M}$. It should be noted that, due to the symmetry of the considered flow problem, the ensemble-averaged statistics are axisymmetric, so they are not dependent on the azimuthal coordinate, as indicated in the left-hand side of Eq. (3). All statistics were computed on the fly during the simulations, with the purpose of minimizing the storage requirements and maximizing the size of the statistical sample, including all instantaneous realizations of the solution during ten revolutions of the turbine, after development of statistically steady conditions. This way about 40 000 flow fields were utilized for the computation of the statistics for each case.

The ensemble-averaged root-mean-squares were computed as

$$\bar{\mathscr{Q}}'(r,z) = \sqrt{\frac{1}{\mathbb{M}}\sum_{i=1}^{\mathbb{M}}[\mathscr{Q}(r,\vartheta,z,t_i)]^2 - \left[\bar{\mathscr{Q}}(r,z)\right]^2}. \quad (4)$$

They were utilized to evaluate the ensemble-averaged turbulent kinetic energy as

$$\bar{k}(r,z) = \frac{1}{2}\left\{[\bar{u}_r'(r,z)]^2 + [\bar{u}_\vartheta'(r,z)]^2 + [\bar{u}_z'(r,z)]^2\right\}, \quad (5)$$

where $\bar{u}_r'$, $\bar{u}_\vartheta'$, and $\bar{u}_z'$ are the ensemble-averaged root-mean-squares for the radial, azimuthal, and axial velocity components, respectively. The phase-averages were defined as

$$\widehat{\mathscr{Q}}(r,\vartheta,z) = \frac{1}{\mathbb{N}}\sum_{i=1}^{\mathbb{N}}\mathscr{Q}(r,\vartheta+t_i\Omega,z,t_i), \quad (6)$$

where $\mathbb{N}$ is the size of the statistical sample. Notice that since phase-averages were sampled on the fly on a grid rotating with the turbine, also for them all instantaneous realizations of the solution, after the initial transient, were utilized. Therefore, $\mathbb{N}$ was equal to $\mathbb{M}$. It is also worth noting that, in contrast with the ensemble-averaged statistics, the phase-averaged ones are not axisymmetric, keeping instead the periodicity of 120° of the turbine geometry.

The phase-averaged root-mean-squares were computed as

$$\widehat{\mathscr{Q}}'(r,\vartheta,z) = \sqrt{\frac{1}{\mathbb{N}}\sum_{i=1}^{\mathbb{N}}[\mathscr{Q}(r,\vartheta+t_i\Omega,z,t_i)]^2 - \left[\widehat{\mathscr{Q}}(r,\vartheta,z)\right]^2}. \quad (7)$$

They allowed calculating the phase-averaged turbulent kinetic energy as

$$\widehat{k}(r,\vartheta,z) = \frac{1}{2}\left\{[\widehat{u}_r'(r,\vartheta,z)]^2 + [\widehat{u}_\vartheta'(r,\vartheta,z)]^2 + [\widehat{u}_z'(r,\vartheta,z)]^2\right\}, \quad (8)$$

where $\widehat{u}_r'$, $\widehat{u}_\vartheta'$, and $\widehat{u}_z'$ are the phase-averaged root-mean-squares for the radial, azimuthal, and axial velocity components, respectively.

B. Instability of the tip vortices

The analysis reported by Posa and Broglia[51,52] and Posa, Broglia, and Balaras,[58] dealing with the wake of the isolated turbine, pointed out the importance of the instability of the tip vortices in the process of wake recovery. Wake contraction and momentum replenishment downstream of the turbine start when the helical vortices originating from the tip of the blades breakup. The present simulations demonstrated that the disturbance of the inflow conditions produced by an upstream turbine affects substantially this process. This is shown in Fig. 5, where instantaneous visualizations of the tip vortices are provided, using contours of the second invariant of the velocity gradient tensor, Q. For the case of an isolated turbine operating within a uniform inflow, the system of tip vortices keeps stable and coherent across a relatively large distance downstream, corresponding to about two diameters from the rotor plane. Instabilities develop initially as deviations from the original helical trajectory. They produce mutual inductance between helices, triggering further instability and leading to leapfrogging, meandering and eventually breakup of the tip vortices. These phenomena are illustrated in the visualization of Fig. 5(a),

dealing with the computation carried out on the isolated turbine. However, they occur much closer to the rotor plane for all other cases when the turbine operates in the wake of another turbine. A weak sensitivity to the distance from the upstream turbine is shown across cases, compared to the dramatic change from the visualization in Fig. 5(a), as demonstrated by the other panels of Fig. 5, referring to the cases **DT10**, **DT8**, and **DT6**, respectively: although an increasingly faster destabilization of the system of tip vortices is distinguishable from Figs. 5(b)–5(d), for all cases, it occurs much earlier, compared to that illustrated in Fig. 5(a). This result is consistent with the theoretical analysis and experiments on the instability of helical vortices reported by Quaranta et al.[75,76] They demonstrated that even small perturbations are able to trigger instability, which explains in the present case the dramatic change from the case of a rotor working within a uniform flow. As discussed in detail below, this earlier instability, compared to the behavior observed downstream of the isolated turbine, is actually beneficial in promoting a faster wake recovery.

The visualizations of Fig. 5 allow capturing also the fine grain structures produced by the process of instability of the large tip vortices. Already in the case of the isolated turbine [see Fig. 5(a)], it is clear that the breakup of the tip vortices starts the contraction of the wake and the formation of smaller structures, in agreement with the findings from laboratory experiments in the wake of a wind turbine reported by Lignarolo et al.[77,78] This is the signature of the process of energy cascade from large toward small structures, typical of turbulence. The study on the turbine immersed within a uniform flow by Posa and Broglia[52] demonstrated, indeed, that turbulent transport plays a major role in the process of wake recovery, contributing to the penetration of the free-stream momentum into the wake core. The comparison against the bottom panels of the same figure is very interesting. It is evident that wake contraction starts much earlier when the turbine works in the wake of an upstream one. In addition, the density of the small structures originating from the breakup of the tip vortices is obviously higher, compared to that seen in Fig. 5(a). This is a clue of the increased importance of turbulent transport in the process of recovery of the near wake of the turbine, as discussed more quantitatively later. It is also interesting to notice in Fig. 5 that the substantial increase of the density of the small structures in the near wake of the downstream turbines comes mostly from faster instability, rather than from the wake of the upstream turbine. This can be inferred looking in Fig. 5 at the region just upstream of the rotor plane.

A more quantitative comparison across cases is reported in Fig. 6, where the power spectral densities of the time-history for the radial, azimuthal, and axial velocity components are reported at a probe placed in the wake of each turbine at the radial coordinate $r/D = 0.6$ and the streamwise coordinate $z/D = 0.5$. The radial position of the probe was selected to take into account the initial expansion of the wake just downstream of the rotor plane. Evident peaks are distinguishable in the case of the isolated turbine at the frequency of the blade passage, f_{bp}, and its higher harmonics. They are associated with the periodic passage of the vortices shed from the tip of each blade. This is not the case for all downstream turbines. These results are consistent with the above discussion, pointing to the earlier instability of the tip vortices, caused by the perturbation of the inflow conditions. In addition, for the downstream turbines, higher values of energy at frequencies other than that of the blade passage and its higher harmonics
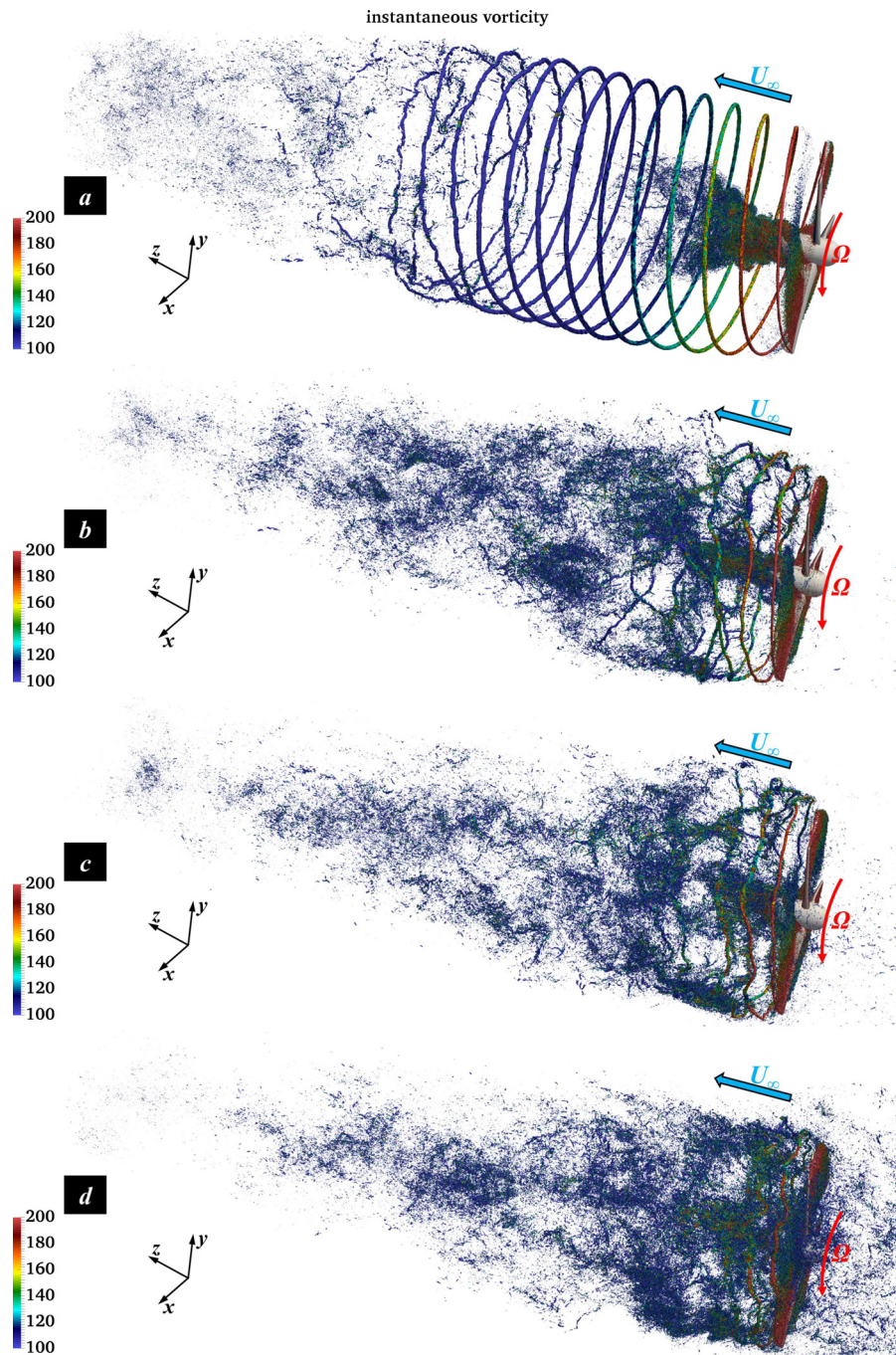
instantaneous vorticity

FIG. 5. Instantaneous isosurfaces of the second invariant of the velocity gradient tensor, $QD^2/U_\infty^2 = 2,000$, colored by vorticity magnitude: *IST* (a), *DT*10 (b), *DT*8 (c), and *DT*6 (d). Vorticity values scaled by U_∞/D.

are visible in Fig. 6. This can be explained by the contribution of turbulence coming from upstream, directly associated with the inflow ingested by the turbine, and especially by the earlier instability of the tip vortices, distributing their energy across the entire range of frequencies. It is worth noting that differences across cases of downstream turbines are rather small if compared with those from the spectra for **IST**, confirming that turbulence levels and the process of

instability of the wake are a weak function of the distance from the upstream turbine, at least in the range of distances considered in the present study.

In Fig. 6, also the slope within the inertial range of frequencies for the homogeneous, isotropic turbulence is represented by a dashed line. Its comparison with the power spectral densities from the present simulations points out that (i) in all cases, the expected behavior of
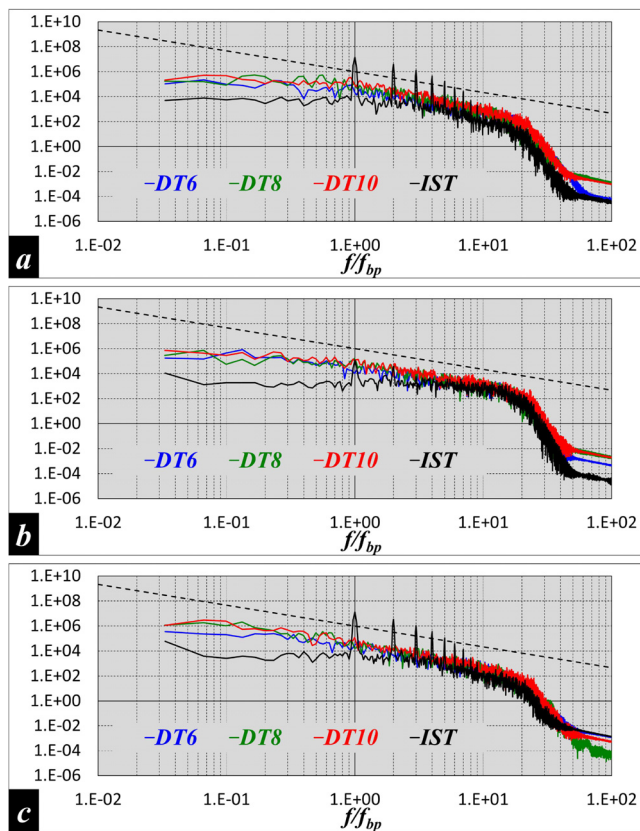
FIG. 6. Power spectral densities of the time-history of the radial (a), azimuthal (b), and axial (c) velocity components at a probe placed downstream of the rotor plane at the radial coordinate $r/D = 0.6$ and the axial coordinate $z/D = 0.5$: comparison across cases. In each panel, the dashed line representing the slope within the inertial range of frequencies from Kolmogorov's theory on homogeneous, isotropic turbulence.

turbulence is properly captured across a wide range of frequencies, giving confidence on the adequacy of the adopted methodology and level of grid resolution in tackling the complex phenomena affecting the wake turbulence; (ii) the typical trend of the homogeneous, isotropic turbulence is reproduced across a wider range of scales in the wake of the downstream turbines. Since the same grid resolution was adopted for all cases, the latter result provides additional evidence that the process of wake development is at a more advanced stage for **DT**10, **DT**8, and **DT**6, compared to **IST**, resulting in a more significant redistribution of the energy of the tip vortices across all frequencies.

C. Wake recovery

In this section, comparisons will be presented across the downstream turbines and the isolated turbine in terms of wake recovery. Figure 7 deals with the contours of the ensemble-averaged streamwise velocity on a meridian plane through the axis of the turbines. In the same visualizations, the isolines represent locations where the ensemble-averaged streamwise velocity is equal to zero, isolating regions of reverse flow. It is very clear that the velocity deficit in the

wake of the downstream turbines experiences a much faster decrease, compared to the isolated turbine. This result is in agreement with those on two aligned hydrokinetic turbines, working in conditions of low environmental turbulence, from the flume tank measurements by Mycek *et al.,*[42,74] They demonstrated that the wake recovery of the downstream turbine was much faster than that of the upstream one. Similar results were recently reported by Okulov *et al.,*[12] who conducted experiments on linear arrays consisting of up to four hydrokinetic turbines. They also observed a faster development of the wake of the second turbine, in comparison with the first one, while for the third and the fourth ones, the velocity fields were not modified substantially from those of the second turbine. In addition, the development of the wakes of the downstream turbines in Fig. 7 is rather similar across cases, despite the substantial differences affecting the inflow conditions, as visible in the region just upstream of the rotor plane. Actually, the speed of the wake recovery is even a slightly decreasing function of the distance from the upstream turbine: it is the fastest in the **DT**6 case, experiencing by far the lowest velocities at the inflow of the turbine, whilst it is the slowest in the **DT**10 case. As discussed above, this result depends on the ability of the wake of the upstream turbine of triggering a faster destabilization of the system of tip vortices shed by the downstream turbine. Figure 7 also shows that the upstream flow is affected significantly by the downstream turbine. The latter decelerates the incoming flow, preventing the recovery of the wake of the upstream turbine. As a result, the momentum ingested by the closest turbine is the lowest one, which is the reason of the decreasing levels of thrust and power coefficients for decreasing distances from the upstream turbine, discussed in our earlier work.[53]

The speed of wake recovery is represented more quantitatively in Fig. 8, where the streamwise evolution of the ensemble-averaged deficit of streamwise momentum (relative to the free-stream) is reported. It was computed as

$$\Delta \bar{M}_z(z) = \int_A \Delta \bar{m}_z(r, \vartheta, z) dS = 2\pi \int_{r=0}^{r=R} \Delta \bar{m}_z(r, z) dr. \quad (9)$$

Equation (9) takes into account that the ensemble-averaged fields are axisysmmetric, while $\Delta \bar{m}_z$ is the deficit of streamwise momentum per unit area. It was defined as

$$\Delta \bar{m}_z(r, z) = \rho \left[U_\infty^2 - \bar{u}_z(r, z) \left| \bar{u}_z(r, z) \right| \right], \quad (10)$$

where the absolute value of the ensemble-averaged streamwise velocity was considered, to take properly into account the contribution by regions of reverse flow within the wake.

In Fig. 8, while the momentum deficit, relative to the free-stream, is not equal to zero upstream of the rotor plane in the cases **DT**6, **DT**8, and **DT**10, in contrast with **IST**, its decrease downstream is much faster. In particular, just upstream of $z/D = 0$, there is an increase, due to the blockage produced by the turbine, affecting all cases. Downstream of the isolated turbine, the momentum deficit keeps growing, which is due to the expansion of the wake outward from the extraction area, that is the frontal area of the rotor. This effect is much milder for all downstream turbines. In addition, it is also interesting to observe that the deficit just downstream of all turbines operating within the upstream wake is very similar, demonstrating that the momentum they are able to extract is an increasing function of the one they ingest at the inflow. This result is obviously consistent
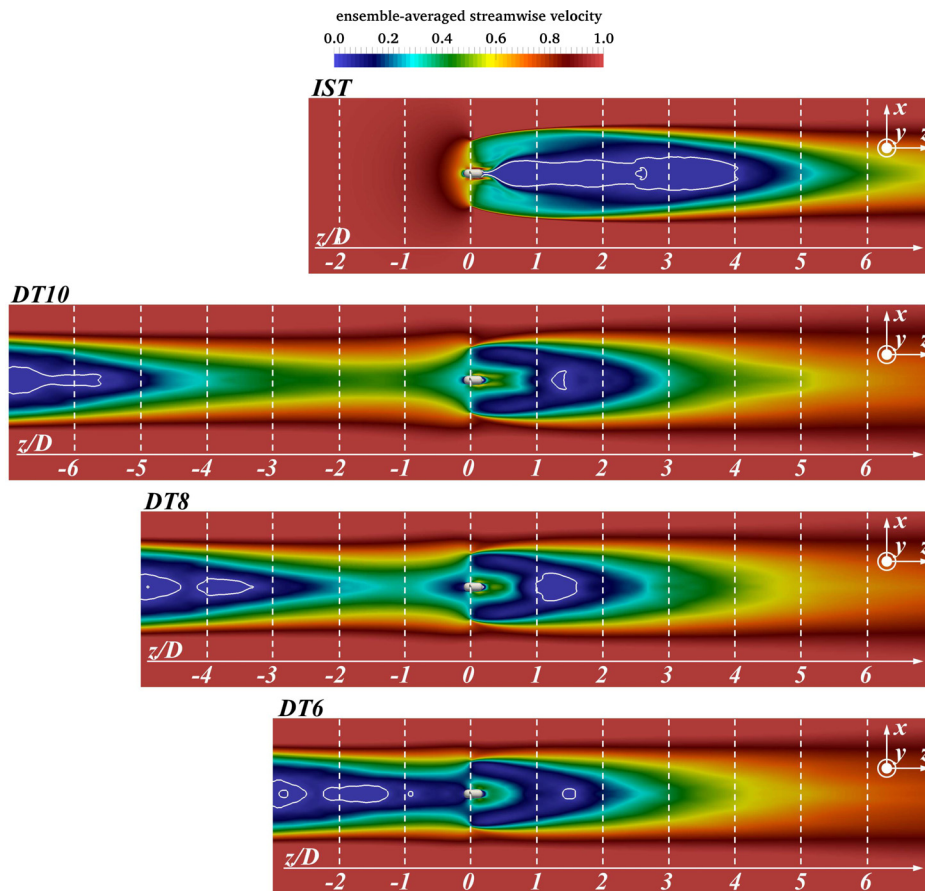
FIG. 7. Contours of ensemble-averaged streamwise velocity on a meridian plane through the axis of the turbines. From top to bottom cases, *IST*, *DT10*, *DT8*, and *DT6*, respectively. Isolines for $\bar{u}_z = 0$. Values scaled by the free-stream velocity, U_∞.

with the strong dependence of the performance of the downstream turbines on their distance from the upstream one.[53] Then, while the instability of the system of tip vortices takes about three diameters downstream of the isolated turbine to trigger the process of wake recovery, it occurs much earlier in all other cases: already at about one diameter from the rotor plane, the momentum deficit starts decreasing. As shown by the contours of streamwise velocity, the dependence

of the speed of wake recovery on the position within the wake of the upstream turbine is rather weak, with the case *DT6*, dealing with the closest turbine, displaying a slightly faster momentum replenishment.

The process of recovery is tied to instabilities of the tip vortices at the outer boundary of the wake, which allow influx of momentum from the free-stream into the wake core, thanks to radial flows. This is demonstrated in Fig. 9 by means of contours of ensemble-averaged
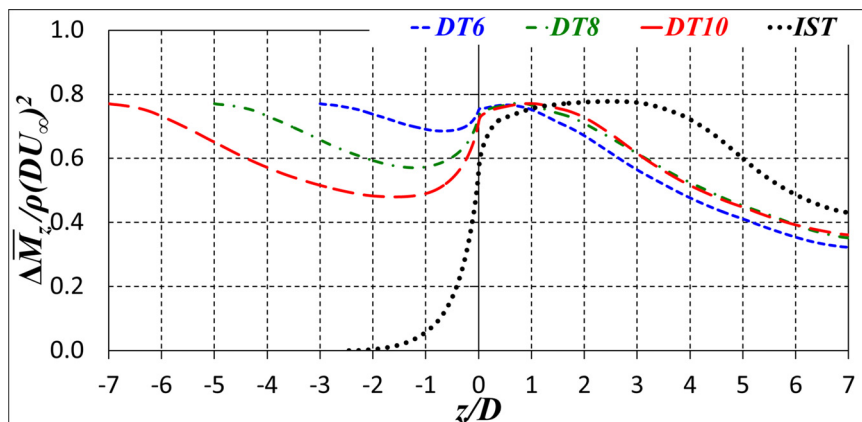

FIG. 8. Streamwise evolution of deficit of streamwise momentum through the extraction area of the turbine, relative to the free-stream, computed from the ensemble-averaged solution of the flow. Comparison across configurations.
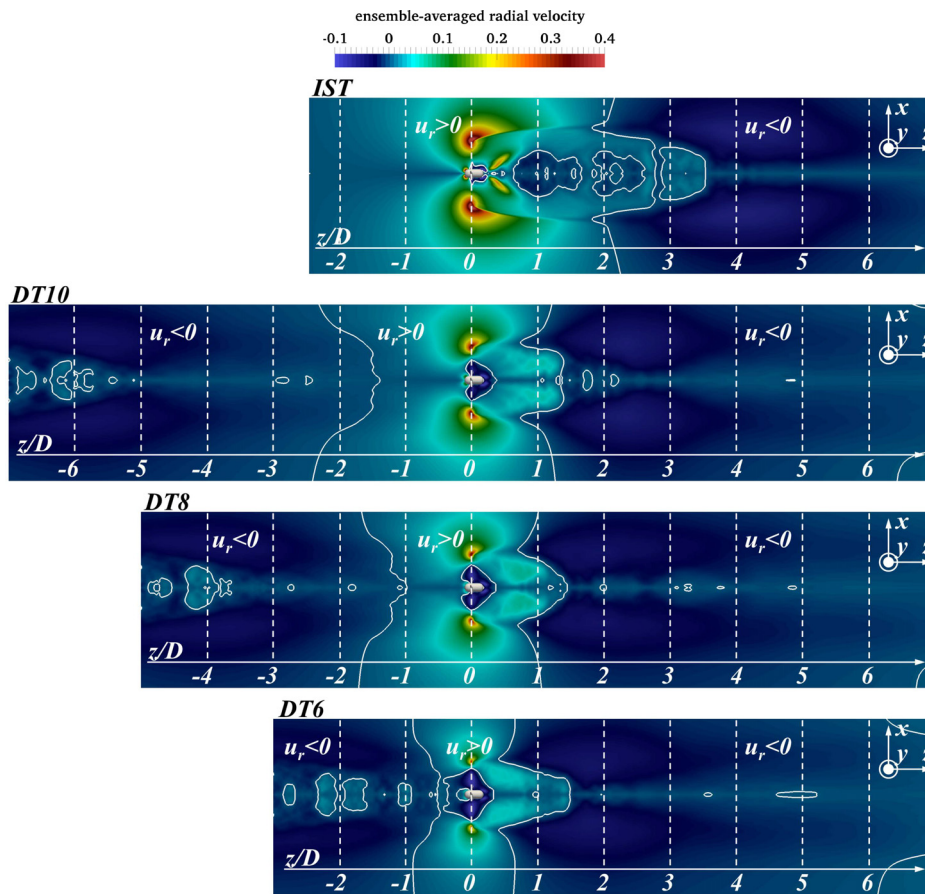
FIG. 9. Contours of ensemble-averaged radial velocity on a meridian plane through the axis of the turbines. From top to bottom cases, *IST*, *DT*10, *DT*8, and *DT*6, respectively. Isolines for $\bar{u}_r = 0$. Values scaled by the free-stream velocity, U_∞.

radial velocity. In the top panel of Fig. 9, referring to the case of an isolated turbine operating in a uniform inflow, the values of radial velocity in the near wake are positive, which is consistent with the above discussion, dealing with wake expansion. However, the instability of the wake system triggers negative values of radial velocity, whose peaks at about $z/D = 4.5$ correlate well with the location of the fastest rate of wake recovery illustrated in Fig. 8. Actually, this phenomenon is visible in all panels of Fig. 9. However, when the turbine operates in the wake of another turbine, generating a perturbation of its inflow conditions, an upstream displacement of the negative maxima of radial velocity occurs, which is the result of a faster destabilization of its wake system. Again, this behavior is actually quite similar across all cases with different locations within the wake of the upstream turbine, which is in agreement with the similarity observed above also on the streamwise evolution of the momentum deficit: positive radial velocities on the rotor plane are smaller than for the isolated turbine and extend over shorter distances downstream, with the isolines separating the regions of positive and negative radial velocities in Fig. 9 moving upstream. In agreement with Fig. 7, this displacement is slightly more significant for shorter distances from the upstream turbine, resulting in a slightly faster wake recovery. These results are in line with the studies available in the literature on the influence by the environmental turbulence on wake recovery since the wake of the upstream turbine results in higher levels of turbulence ingested by the downstream

one. For instance, the experiments reported by Mycek *et al.,*[42,74] Vinod and Banerjee,[79] and Gaurier *et al.*[10] demonstrated that higher levels of free-stream turbulence are able to accelerate the process of wake development, through a faster breakup of the coherence of the tip vortices.

Also for the ensemble-averaged radial velocity more quantitative comparisons across cases are provided in Fig. 10. Figure 10(a) deals with its streamwise evolution at the boundary of the extraction area, corresponding to the radial location $r = R$. At the rotor plane, a strong positive peak is produced. The radial velocity keeps positive values up to almost three diameters downstream of the isolated turbine, while achieves its negative peak at about $z/D = 4.5$. Then, its gradual decrease is due to the depletion of the radial gradients, as a consequence of wake recovery. For the downstream turbines, negative radial velocities at the boundary of their extraction area occur much earlier. This is the case also for their decline, which is the consequence of the faster wake recovery.

A more global overview of the radial flows within the wake is provided in the panel of Fig. 10(b), where the average of the radial velocity across the whole extraction area is considered. In Fig. 10(b), even more than in Fig. 10(a), the deviations affecting the upstream behaviors point to the largest deceleration of the flow by the isolated turbine and the smallest one in the case of the closest downstream turbine, correlating with the largest and smallest power extractions from
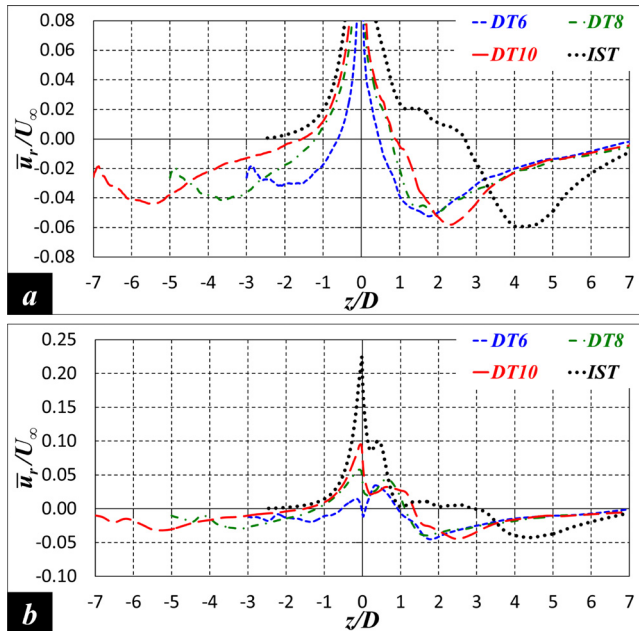
FIG. 10. Streamwise evolution of the ensemble-averaged radial velocity: (a) at the boundary of the extraction area ($r = R$) and (b) average over the extraction area ($0 \leq r \leq R$). Comparison across configurations.

the flow, respectively. The radial velocity switches its sign slightly more downstream of the rotor plane than in Fig. 10(a) since inward radial flows start at the wake boundary and then gradually propagate toward the wake core. Nonetheless, the behaviors observed in Fig. 10(b) are similar to those in Fig. 10(a): wake contraction is much faster for *DT*10, *DT*8, and *DT*6 than for *IST*, while the distance from the upstream turbine has a milder influence on its speed.

Figure 11 shows phase-averaged contours of turbulent kinetic energy. Since they are able to isolate the signature of the tip vortices, they are well suited to highlight the faster destabilization produced by the wake of an upstream turbine. In addition, as discussed later, turbulence plays an important role in the process of wake recovery. The top panel of Fig. 11, dealing with the case of an isolated turbine, demonstrates the presence of very coherent tip vortices at the outer boundary of the wake. The signature of their cores is very well distinguishable in the local maxima originating from the tip of the blades. When instability develops, those maxima are replaced by a wide, diffused region of large turbulence, spreading radially and bending toward the wake core. The contours in all other panels of Fig. 11 deviate substantially from those in the top panel. It is clear that the instability of the tip vortices occurs much closer to the plane of the turbine and is rather insensitive to its position within the wake of the upstream one. However, it is interesting to notice that the values at the outer boundary are higher when the downstream turbine is placed further away: it ingests a higher-momentum flow, thus its blades are more highly loaded, resulting in stronger tip vortices and higher levels of turbulent kinetic energy originating from their instability.

In Fig. 12(a), the streamwise evolution of the ensemble-averaged turbulent kinetic energy is shown at the boundary of the extraction area. The maxima at downstream locations in Fig. 12(a) correlate with

the ones of negative radial velocity shown in Fig. 10(a). It is worth noting that, just downstream of the isolated turbine, the values of turbulent kinetic energy are close to zero, since the wake boundary is displaced toward outer radial coordinates due to wake expansion. This is more limited in the cases of the downstream turbines. For them, the increase of turbulence, due to instability of the tip vortices, occurs just downstream of the rotor plane, at a location that is hardly dependent on the distance from the upstream turbine. The maxima achieved in those cases are also higher than that in the wake of the isolated turbine, which is the likely consequence of the earlier instability of the tip vortices, where they are characterized by higher levels of circulation within their core. As discussed above, the lower peak for *DT*6 can be explained by the weaker tip vortices generated in that case, compared to *DT*8 and *DT*10, being the blades of the turbine more lightly loaded, as a result of the lower momentum at the inflow. It is interesting to notice that *DT*6 experiences lower turbulence at the boundary of the extraction area, even if the ingested one is higher. Nonetheless, also the comparison in Fig. 12(a) confirms that the major differences occur between the cases of the downstream turbines and the one of the isolated turbine. This conclusion is reinforced in the panel of Fig. 12(b), dealing with the average of the ensemble-averaged turbulent kinetic energy across the extraction area. The streamwise evolution is very close across *DT*6, *DT*8, and *DT*10, showing substantially higher values than *IST* and a much faster rise of turbulence levels downstream of the rotor plane. It is worth noting, especially for the case of the isolated turbine, the presence of a small bump in the streamwise evolution of turbulent kinetic energy, at about $z/D = 5.0$, which is also visible in the contours of Fig. 11. It is actually caused by the acceleration of grid coarsening, occurring in the vicinity of the outflow boundary of the computational domain.

D. Analysis of the momentum balance

In this section, the comparison is extended to the analysis of the ensemble-averaged terms of the streamwise component of the momentum equation, providing details on the phenomena leading the process of wake recovery, as recently reported in the fields of wind energy[80,81] and cross-flow turbines[82–86]

$$\bar{u}_r \frac{\partial \bar{u}_z}{\partial r} + \frac{\bar{u}_\vartheta}{r}\frac{\partial \bar{u}_z}{\partial \vartheta} + \bar{u}_z \frac{\partial \bar{u}_z}{\partial z} + \frac{\partial \overline{u'_r u'_z}}{\partial r} + \frac{1}{r}\frac{\partial \overline{u'_\vartheta u'_z}}{\partial \vartheta} + \frac{\partial \overline{u'_z u'_z}}{\partial z}$$
$$= -\frac{\partial \bar{p}}{\partial z} + \frac{1}{Re}\left[\frac{1}{r}\frac{\partial}{\partial r}\left(r\frac{\partial \bar{u}_z}{\partial r}\right) + \frac{1}{r^2}\frac{\partial^2 \bar{u}_z}{\partial \vartheta^2} + \frac{\partial^2 \bar{u}_z}{\partial z^2}\right] - D(\bar{\tau}_{zj}). \quad (11)$$

Taking into account that the ensemble-average of all terms of azimuthal derivative is equal to zero, Eq. (11) can be simplified into

$$\bar{u}_z \frac{\partial \bar{u}_z}{\partial z} = -\bar{u}_r \frac{\partial \bar{u}_z}{\partial r} - \frac{\partial \overline{u'_r u'_z}}{\partial r} - \frac{\partial \overline{u'_z u'_z}}{\partial z} - \frac{\partial \bar{p}}{\partial z}$$
$$+ \frac{1}{Re}\left[\frac{1}{r}\frac{\partial}{\partial r}\left(r\frac{\partial \bar{u}_z}{\partial r}\right) + \frac{\partial^2 \bar{u}_z}{\partial z^2}\right] - D(\bar{\tau}_{zj}). \quad (12)$$

In the following discussion, the quantities in Eq. (12) will be indicated, respectively, as overall transport of streamwise momentum (σ), radial advection (σ_1), radial turbulent transport (σ_2), streamwise turbulent transport (σ_3), pressure transport (σ_4), viscous diffusion (σ_5), and modeled turbulent transport (σ_6). It should be noted that σ_5 was verified always negligible, as expected.
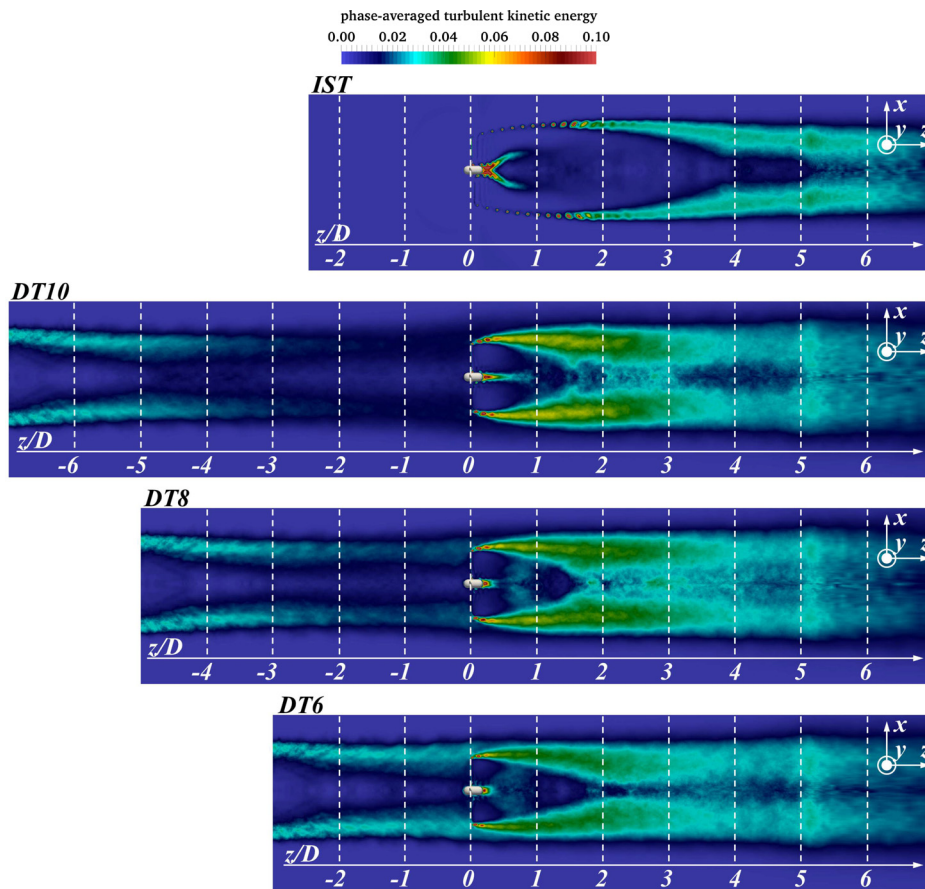
FIG. 11. Contours of phase-averaged turbulent kinetic energy on a meridian plane through the axis of the turbines. From top to bottom cases, *IST*, *DT*10, *DT*8, and *DT*6, respectively. Values scaled by the square of the free-stream velocity, U_∞^2.

Also for the analysis of the momentum balance equation an integral approach was adopted, considering the average across the projection of the extraction area of the turbine downstream of its plane

$$\Sigma(z) = \frac{1}{A}\int_A \sigma(r,\vartheta,z)dS = \frac{1}{R}\int_{r=0}^{r=R}\sigma(r,z)dr, \qquad (13)$$

where the axisymmetry of the ensemble-averages was taken into account.

Results are provided in Fig. 13, dealing with the streamwise location at $z/D = 1.0$. In Fig. 13(a), the overall transport, Σ, is considered. The comparison is clear: while the momentum in the wake of the isolated turbine is still decreasing, this is not the case for all downstream turbines. In particular, the closer they are to the upstream turbine, the faster the process of momentum replenishment. The other panels in Fig. 13 deal with the major terms of the RHS of Eq. (12). In Fig. 13(b), the results for radial advection are reported. Actually, at this streamwise location, radial advection is contributing substantially to wake recovery in the case *DT*6 only. This is due to its earlier instability, producing inward radial flows and wake contraction. However, the process of instability, promoting wake recovery, already started also for *DT*10 and *DT*8, as demonstrated in Fig. 13(c), where the contribution by radial turbulent transport is shown. Turbulent mixing, resulting from the breakup of the tip vortices, was also found the trigger of the process of wake recovery through kinetic energy transport across the

outer wake boundary downstream of wind turbines.[77,78] The latter is negligible for *IST* since the tip vortices shed from the blades of the turbine are still very coherent and stable in that case. At $z/D = 1.0$, also the role of pressure transport is significant, as demonstrated in Fig. 13(d): it is negative and rather uniform across cases.

Figure 14 shows results at $z/D = 3.0$, which is roughly the position where Σ achieves its maximum for all cases of downstream turbines. In particular, Fig. 14(a) demonstrates that their values of Σ are substantially higher than that for *IST*, whose process of wake recovery is shifted to more downstream coordinates. The value of Σ here is slightly higher for *DT*10, since *DT*8 and *DT*6 actually achieved their maxima at slightly upstream positions within the wake. At this streamwise location, radial advection [Fig. 14(b)] still plays a less significant role for *IST* since the process of wake instability in this case is delayed. However, the radial turbulent transport is already rather significant also downstream of the isolated turbine, as shown in Fig. 14(c), since the instability of the tip vortices for the isolated turbine eventually developed at about $z/D = 2.0$. However, at $z/D = 3.0$, the computational grid is coarser than in the vicinity of the rotor plane, so, the contribution by SGS modeling is important. This is included in the overall turbulent transport, illustrated in Fig. 14(d): it is shown that for the downstream turbines, turbulent transport is the major source of wake recovery, being the instability of the wake system fully developed and the contribution by radial advection limited by the depletion of the
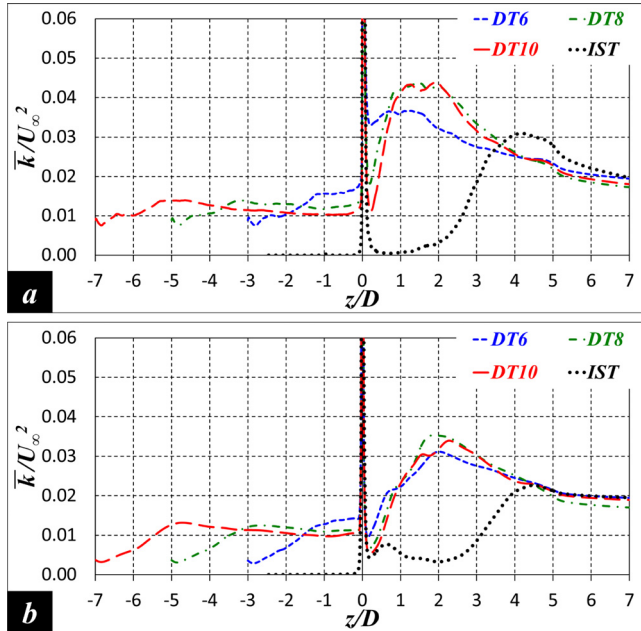
FIG. 12. Streamwise evolution of the ensemble-averaged turbulent kinetic energy: (a) at the boundary of the extraction area ($r = R$) and (b) average over the extraction area ($0 \leq r \leq R$). Comparison across configurations.

FIG. 13. Terms of the momentum balance equation at $z/D = 1.0$, averaged across the projection of the extraction area of the turbine: overall transport (a), radial advection (b), radial turbulent transport (c), and pressure transport (d).

radial gradients because of the upstream recovery of streamwise momentum.

The analysis conducted in the wake of the isolated turbine[52] pointed out that the process of wake recovery is not uniform across the radial direction. Therefore, in the following the quantities:

$$\Sigma^{\text{inner}}(z) = \frac{1}{A^{\text{inner}}} \int_{A^{\text{inner}}} \sigma(r, \vartheta, z) dS = \frac{1}{0.5R} \int_{r=0}^{r=0.5R} \sigma(r, z) dr, \quad (14)$$

$$\Sigma^{\text{outer}}(z) = \frac{1}{A^{\text{outer}}} \int_{A^{\text{outer}}} \sigma(r, \vartheta, z) dS = \frac{1}{0.5R} \int_{r=0.5R}^{r=R} \sigma(r, z) dr, \quad (15)$$

will be compared. They are the averages of the terms contributing to the momentum balance at the inner and outer radii of the wake, respectively.

Figure 15 reports the comparison between inner and outer radii at $z/D = 1.0$, whose results are represented in the left and right columns in each panel, respectively. Figure 15(a) is very clear in showing that the process of wake recovery is not uniform across the radial direction. In particular, all cases still experience negative values of Σ^{inner}, while the outer radii are consistent with the global behavior observed above in Fig. 13(a). Therefore, Fig. 15(a) highlights that just downstream of the rotor plane the influence by the wake from an upstream turbine is able to trigger a faster recovery at the outer radii, while this is still not the case at the inner ones, which are actually experiencing an increase of the momentum deficit across the streamwise direction. The especially low value of Σ^{inner} for the case **DT10** is due to the expansion by the core of the near wake of the turbine, producing a minimum across the streamwise evolution of Σ^{inner}. Actually, this behavior was verified also for **DT8** and **DT6**, but in those cases, it

occurs slightly more upstream, shifting the minimum for Σ^{inner} to smaller streamwise coordinates.

The panel in Fig. 15(b) shows that the contribution by radial advection is substantially different across cases. It is clear that for **DT6**
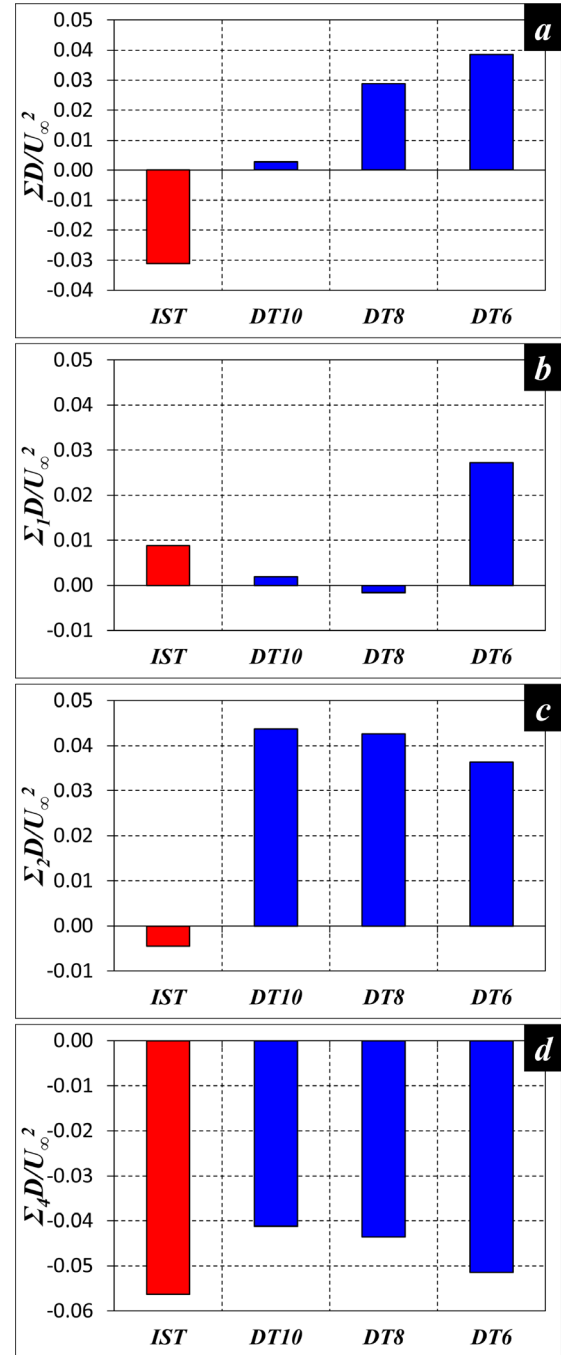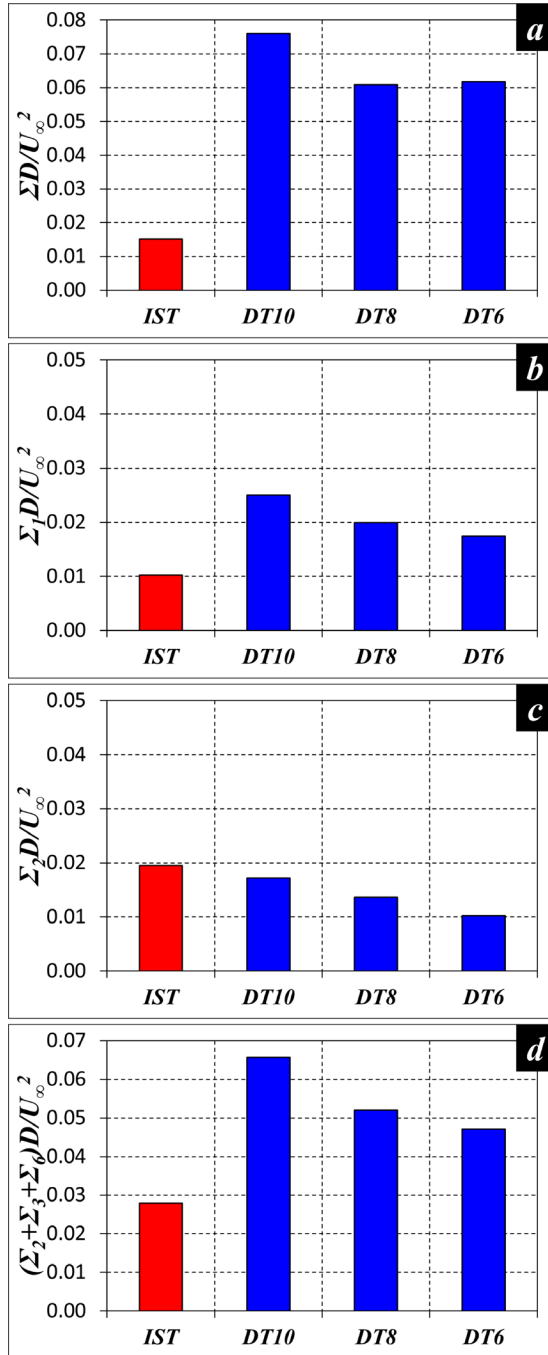
FIG. 14. Terms of the momentum balance equation at $z/D = 3.0$, averaged across the projection of the extraction area of the turbine: overall transport (a), radial advection (b), radial turbulent transport (c), and total turbulent transport (d).

FIG. 15. Terms of the momentum balance equation at $z/D = 1.0$, averaged across the projections of the inner and outer extraction areas of the turbine (left and right columns in each panel, respectively), as defined in Eqs. (14) and (15): overall transport (a), radial advection (b), radial turbulent transport (c), and pressure transport (d).

radial advection is producing a significant recovery in the outer region of the wake, whilst its role in the inner wake is still very limited. This is the case within both inner and outer wakes for **DT8**, whose contraction begins slightly more downstream. The results for **DT10** deserve
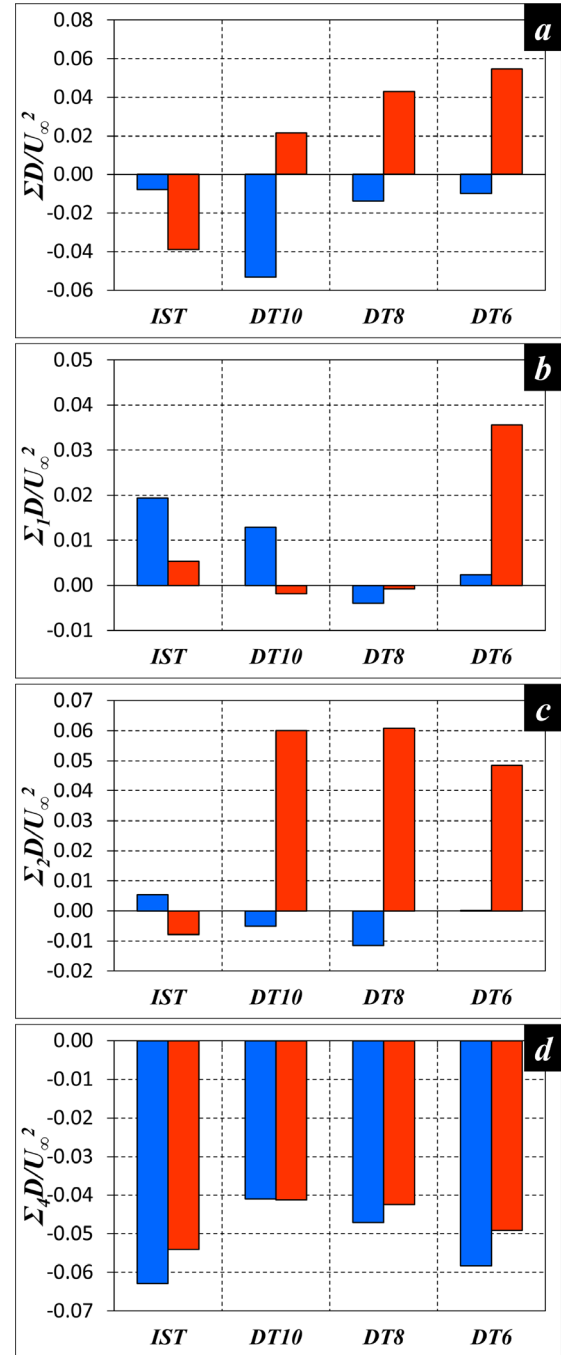
more attention. The positive value of the quantity Σ_1^{inner} is due to a non-monotonic radial evolution of the streamwise velocity, resulting at the boundary between the inner and the outer wakes ($r = 0.5R$) in negative values for $\partial \bar{u}_z / \partial r$ and producing positive values of $-\bar{u}_r \, \partial \bar{u}_z / \partial r$,

due to the expansion of the wake core ($\bar{u}_r > 0$). As discussed above, this is a behavior also occurring for **DT8** and **DT6**, but slightly more upstream. In contrast, the positive values of Σ_1^{inner} for the isolated turbine are due to the contraction of the inner wake, occurring downstream of the expansion of the hub vortex just behind the turbine. Therefore, for both **DT10** and **IST** in Fig. 15(b), the positive values of Σ_1^{inner} are actually not associated with phenomena of wake recovery via supply of momentum from the free-stream. They come instead from the complex topology of the flow within the core of the near wake.

Figure 15(c), dealing with the radial turbulent transport, is even more explicit in pointing that, while the instability of the tip vortices is already promoting a significant recovery of the outer wake, in a similar way across downstream turbines, this process does not involve the wake core yet. Figure 15(d) demonstrates that, in contrast with the other terms contributing to the balance of streamwise momentum, pressure transport is rather uniform across the radial direction. Its role within the near wake is obviously quite significant.

Figure 16 deals with similar comparisons, but at the streamwise coordinate $z/D = 3.0$. Figure 16(a) shows that for the downstream turbines recovery by supply of streamwise momentum from the free-stream reached also the inner wake. There Σ is even slightly higher within the wake core since the process is at a more advanced stage at the outer radii. Across both inner and outer wakes, the rate of recovery of streamwise momentum is rather uniform across all downstream turbines. As discussed above for the average over the whole extraction area, the values of Σ^{inner} and Σ^{outer} are slightly higher for **DT10** than for **DT8** and **DT6** since the peak of their streamwise evolution shifts slightly more upstream as the distance from the upstream turbine is reduced. It is evident that for the isolated turbine the process of wake recovery is still at an early stage and practically did not start at the inner radii yet. Figure 16(b) shows that radial advection is the main source of momentum replenishment for the outer region of the wake. This is not the case for the wake core, whose recovery is instead promoted mainly by turbulent transport, as demonstrated in the panels of Figs. 16(c) and 16(d). This is the case for all downstream turbines. Again, the values of turbulent transport for **DT10** in Figs. 16(c) and 16(d) are higher than those for **DT8** and **DT6** since the latter peaked more upstream. In contrast, for the isolated turbine turbulent transport is larger than radial advection also at the outer radii, but this result is due to the process of wake recovery being at its initial stage, so the development of inward radial flows is still limited.

V. CONCLUSIONS

Large-Eddy simulations were conducted, dealing with an axial-flow hydrokinetic turbine, at three positions in the wake of an upstream one. A cylindrical grid consisting of 3.8×10^9 points was utilized, making the present study by far the most well-resolved available in the literature in this class of flows. Results were compared against those of the wake of the same turbine in isolated conditions, operating in a uniform flow. Although direct comparisons with experiments were not available, the trends observed in the present numerical study were verified in close agreement with the results of the experimental studies dealing with aligned axial-flow, hydrokinetic turbines by Mycek et al.,[42] Okulov et al.,[11,12] and Kang et al..[87]

This study is an extension of our earlier work.[53] In particular, we analyzed in detail all terms of the momentum balance
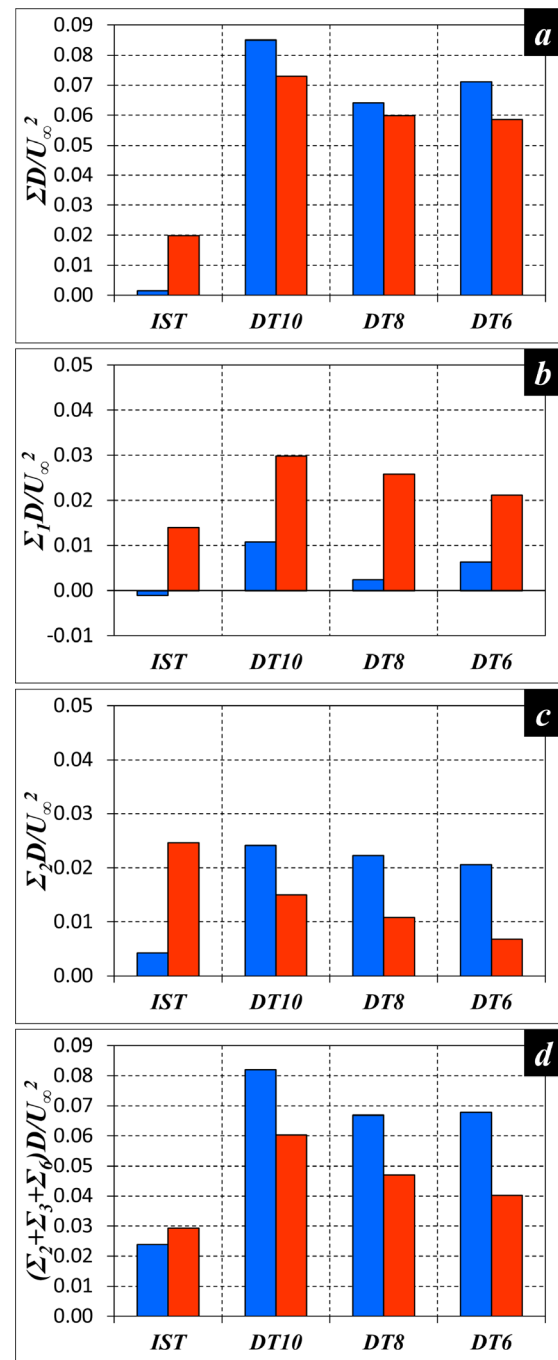

FIG. 16. Terms of the momentum balance equation at $z/D = 3.0$, averaged across the projection of the inner and outer extraction areas of the turbine (left and right columns in each panel, respectively), as defined in Eqs. (14) and (15): overall transport (a), radial advection (b), radial turbulent transport (c), and total turbulent transport (d).

equation and their dependence on the distance of the downstream turbine from the upstream one. From the results of the LES computations reported in this study, we can present the following conclusions:

- The process of wake recovery is strongly tied to the instability of the tip vortices: the latter starts the phenomena of radial advection and turbulent transport at the outer boundary of the wake, enabling replenishment of momentum in the wake core from the free-stream.
- Compared to the case of the isolated turbine in uniform flow, the wake recovery of the downstream turbines features a stronger contribution by radial turbulent transport just downstream of the instability of the tip vortices, accelerating the overall process.
- Even more than for an isolated turbine, wake recovery is dominated at inner radii by turbulent transport. For instance, its contribution at three diameters from the downstream turbines was found between 3 and 4 times higher in comparison with the case of the same turbine operating within the free-stream: turbulent transport allows accelerating the momentum replenishment once the mean radial gradients are mainly depleted.

The implications of these results are important in terms of modeling of the process of wake recovery by lower-fidelity methodologies. For instance, while one can expect that RANS can resolve fairly accurately the momentum transport associated with radial advection and the initial turbulent transport tied to the large scales, that are the tip vortices when they are still coherent, the turbulent transport due to small scales requires to be entirely modeled. Meanwhile, we verified that the latter is very important to complete the process of momentum replenishment downstream of the breakup of the tip vortices. Therefore, it would be important to verify if turbulence models are actually able to mimic accurately this physics, which in arrays of turbines influences the kinetic energy available to downstream devices.

Finally, it should be acknowledged that the supporting stanchion or tower for the actual installation of a hydrokinetic turbine may play an important role in affecting the process of instability of the tip vortices and, in turn, the physics of wake recovery. The support for the rotor is an additional source of momentum deficit downstream of the turbine, but it is also expected to accelerate the instability of the tip vortices and the shear layers at the outer boundary of the wake, starting in advance the phenomena of radial advection and turbulent mixing promoting wake recovery. This effect was not included in the present simulations, which considered the rotor geometry only. In our future studies, it would be interesting to account for it, to explore its influence on the flow physics and assess the accuracy of simulations based on a simplified setup.

AUTHOR DECLARATIONS
Conflict of Interest

The authors have no conflicts to disclose.

Author Contributions

Antonio Posa: Conceptualization (lead), Data curation (lead), Formal analysis (lead), Investigation (lead), Methodology (lead), Project administration (lead), Resources (lead), Software (lead), Supervision (lead), Validation (lead), Visualization (lead), Writing – original draft (lead), and Writing – review & editing (lead). **Riccardo Broglia:** Conceptualization (supporting), Data curation (supporting), Formal analysis (supporting), Investigation (supporting), Methodology (supporting), Project administration (supporting), Resources (supporting), Software (supporting), Supervision (supporting), Validation (supporting), Visualization (supporting), Writing – original draft (supporting), and Writing – review & editing (supporting).

DATA AVAILABILITY

The data that support the findings of this study are available from the corresponding author upon reasonable request.

REFERENCES

[1] A. Hussain, S. Arif, and M. Aslam, "Emerging renewable and sustainable energy technologies: State of the art," Renewable Sustainable Energy Rev. **71**, 12–28 (2017).

[2] N. Laws and B. Epps, "Hydrokinetic energy conversion: Technology, research, and outlook," Renewable Sustainable Energy Rev. **57**, 1245–1259 (2016).

[3] X. Yang, K. Haas, H. Fritz, S. French, X. Shi, V. Neary, and B. Gunawan, "National geodatabase of ocean current power resource in USA," Renewable Sustainable Energy Rev. **44**, 496–507 (2015).

[4] M. Yuce and A. Muratoglu, "Hydrokinetic energy conversion systems: A technology status review," Renewable Sustainable Energy Rev. **43**, 72–82 (2015).

[5] C. Niebuhr, M. van Dijk, V. Neary, and J. Bhagwan, "A review of hydrokinetic turbines and enhancement techniques for canal installations: Technology, applicability and potential," Renewable Sustainable Energy Rev. **113**, 109240 (2019).

[6] L. Jenkins, S. Dreyer, H. Polis, E. Beaver, A. Kowalski, H. Linder, T. McMillin, K. McTiernan, T. Rogier, and L. Wiesebron, "Human dimensions of tidal energy: A review of theories and frameworks," Renewable Sustainable Energy Rev. **97**, 323–337 (2018).

[7] C. Hachmann, T. Stallard, P. Stansby, and B. Lin, "Experimentally validated study of the impact of operating strategies on power efficiency of a turbine array in a bi-directional tidal channel," Renewable Energy **163**, 1408–1426 (2021).

[8] V. Nago, I. Santos, M. Gbedjinou, J. Mensah, G. Tiago Filho, R. Camacho, and R. Barros, "A literature review on wake dissipation length of hydrokinetic turbines as a guide for turbine array configuration," Ocean Eng. **259**, 111863 (2022).

[9] M. Nuernberg and L. Tao, "Experimental study of wake characteristics in tidal turbine arrays," Renewable Energy **127**, 168–181 (2018).

[10] B. Gaurier, C. Carlier, G. Germain, G. Pinon, and E. Rivoalen, "Three tidal turbines in interaction: An experimental study of turbulence intensity effects on wakes and turbine performance," Renewable Energy **148**, 1150–1164 (2020).

[11] V. Okulov, I. Kabardin, I. Litvinov, R. Mikkelsen, I. Naumov, and J. Sørensen, "Wakes and wake interaction between rotors and discs in an experimental model array," J. Phys. **1256**, 012013 (2019).

[12] V. Okulov, I. Naumov, I. Kabardin, I. Litvinov, D. Markovich, R. Mikkelsen, J. Sørensen, S. Alekseenko, and D. Wood, "Experiments on line arrays of horizontal-axis hydroturbines," Renewable Energy **163**, 15–21 (2021).

[13] M. Abolghasemi, M. Piggott, J. Spinneken, A. Viré, C. Cotter, and S. Crammond, "Simulating tidal turbines with multi-scale mesh optimisation techniques," J. Fluids Struct. **66**, 69–90 (2016).

[14] A. Fernandez, "Numerical prediction of the turbulent wakes generated by a row of marine turbines," Int. J. Mar. Energy **16**, 41–50 (2016).

[15] V. Nguyen, S. Guillou, J. Thiébot, and A. Santa Cruz, "Modelling turbulence with an actuator disk representing a tidal turbine," Renewable Energy **97**, 625–635 (2016).

[16] M. Shives and C. Crawford, "Adapted two-equation turbulence closures for actuator disk RANS simulations of wind and tidal turbine wakes," Renewable Energy **92**, 273–292 (2016).

[17] M. Shives and C. Crawford, "Tuned actuator disk approach for predicting tidal turbine performance with wake interaction," Int. J. Mar. Energy **17**, 1–20 (2017).

[18] M. Edmunds, A. Williams, I. Masters, and T. Croft, "An enhanced disk averaged CFD model for the simulation of horizontal axis tidal turbines," Renewable Energy **101**, 67–81 (2017).

[19] M. Edmunds, A. Williams, I. Masters, A. Banerjee, and J. VanZwieten, "A spatially nonlinear generalised actuator disk model for the simulation of horizontal axis wind and tidal turbines," Energy **194**, 116803 (2020).

[20] M. Ahmadi and Z. Yang, "The evolution of turbulence characteristics in the wake of a horizontal axis tidal stream turbine," Renewable Energy **151**, 1008–1015 (2020).

[21] V. Kleine, L. Franceschini, B. Carmo, A. Hanifi, and D. Henningson, "The stability of wakes of floating wind turbines," Phys. Fluids **34**, 074106 (2022).

[22] W.-H. Lam, L. Chen, and R. Hashim, "Analytical wake model of tidal current turbine," Energy **79**, 512–521 (2015).

[23] L. Chen, Y. Yao, and Z.-L. Wang, "Development and validation of a prediction model for the multi-wake of tidal stream turbines," Renewable Energy **155**, 800–809 (2020).

[24] P. Pyakurel, J. VanZwieten, C. Sultan, M. Dhanak, and N. Xiros, "Numerical simulation and dynamical response of a moored hydrokinetic turbine operating in the wake of an upstream turbine for control design," Renewable Energy **114**, 1134–1145 (2017).

[25] A. Brunetti, V. Armenio, and F. Roman, "Large eddy simulation of a marine turbine in a stable stratified flow condition," J. Ocean Eng. Mar. Energy **5**, 1–19 (2019).

[26] C. Gotelli, M. Musa, M. Guala, and C. Escauriaza, "Experimental and numerical investigation of wake interactions of marine hydrokinetic turbines," Energies **12**, 3188 (2019).

[27] J. Sandoval, K. Soto-Rivas, C. Gotelli, and C. Escauriaza, "Modeling the wake dynamics of a marine hydrokinetic turbine using different actuator representations," Ocean Eng. **222**, 108584 (2021).

[28] G. Deng, Z. Zhang, Y. Li, H. Liu, W. Xu, and Y. Pan, "Prospective of development of large-scale tidal current turbine array: An example numerical investigation of Zhejiang, China," Appl. Energy **264**, 114621 (2020).

[29] C. Zhang, J. Zhang, L. Tong, Y. Guo, and P. Zhang, "Investigation of array layout of tidal stream turbines on energy extraction efficiency," Ocean Eng. **196**, 106775 (2020).

[30] O. Lo Brutto, V. Nguyen, S. Guillou, J. Thiébot, and H. Gualous, "Tidal farm analysis using an analytical model for the flow velocity prediction in the wake of a tidal turbine with small diameter to depth ratio," Renewable Energy **99**, 347–359 (2016).

[31] J. Thiébot, S. Guillou, and V. Nguyen, "Modelling the effect of large arrays of tidal turbines with depth-averaged actuator disks," Ocean Eng. **126**, 265–275 (2016).

[32] D. Gajardo, C. Escauriaza, and D. Ingram, "Capturing the development and interactions of wakes in tidal turbine arrays using a coupled BEM-DES model," Ocean Eng. **181**, 71–88 (2019).

[33] C. Liu and C. Hu, "An actuator line - immersed boundary method for simulation of multiple tidal turbines," Renewable Energy **136**, 473–490 (2019).

[34] P. Ouro, L. Ramírez, and M. Harrold, "Analysis of array spacing on tidal stream turbine farm performance using large-eddy simulation," J. Fluids Struct. **91**, 102732 (2019).

[35] N. Lombardi, S. Ordonez-Sanchez, S. Zanforlin, and C. Johnstone, "A hybrid BEM-CFD virtual blade model to predict interactions between tidal stream turbines under wave conditions," J. Mar. Sci. Eng. **8**, 969–919 (2020).

[36] N. Michelet, N. Guillou, G. Chapalain, J. Thiébot, S. Guillou, A. Goward Brown, and S. Neill, "Three-dimensional modelling of turbine wake interactions at a tidal stream energy site," Appl. Ocean Res. **95**, 102009 (2020).

[37] M. Nguyen, H. Jeong, H. Tran, J.-S. Park, and C. Yang, "Energy capture evaluation of tidal current turbines arrays in Uldolmok strait, South Korea," Ocean Eng. **195**, 106675 (2020).

[38] J. Han, J. Jung, and J. Hwang, "Optimal configuration of a tidal current turbine farm in a shallow channel," Ocean Eng. **220**, 108395 (2021).

[39] P. Ouro and T. Nishino, "Performance and wake characteristics of tidal turbines in an infinitely large array," J. Fluid Mech. **925**, A30 (2021).

[40] P. Stansby and P. Ouro, "Modelling marine turbine arrays in tidal flows," J. Hydraul. Res. **60**, 187–204 (2022).

[41] P. Mycek, B. Gaurier, G. Germain, G. Pinon, and E. Rivoalen, "Numerical and experimental study of the interaction between two marine current turbines," Int. J. Mar. Energy **1**, 70–83 (2013).

[42] P. Mycek, B. Gaurier, G. Germain, G. Pinon, and E. Rivoalen, "Experimental study of the turbulence intensity effects on marine current turbines behaviour. Part II: Two interacting turbines," Renewable Energy **68**, 876–892 (2014).

[43] A. Olczak, T. Stallard, T. Feng, and P. Stansby, "Comparison of a RANS blade element model for tidal turbine arrays with laboratory scale measurements of wake velocity and rotor thrust," J. Fluids Struct. **64**, 87–106 (2016).

[44] J. Liu, H. Lin, and S. Purimitla, "Wake field studies of tidal current turbines with different numerical methods," Ocean Eng. **117**, 383–397 (2016).

[45] M. Nuernberg and L. Tao, "Three dimensional tidal turbine array simulations using OpenFOAM with dynamic mesh," Ocean Eng. **147**, 629–646 (2018).

[46] P. Ouro, M. Harrold, T. Stoesser, and P. Bromley, "Hydrodynamic loadings on a horizontal axis tidal turbine prototype," J. Fluids Struct. **71**, 78–95 (2017).

[47] E. Lust, K. Flack, and L. Luznik, "Survey of the near wake of an axial-flow hydrokinetic turbine in quiescent conditions," Renewable Energy **129**, 92–101 (2018).

[48] E. Lust, K. Flack, and L. Luznik, "Survey of the near wake of an axial-flow hydrokinetic turbine in the presence of waves," Renewable Energy **146**, 2199–2209 (2020).

[49] M. Ahmadi, "Influence of upstream turbulence on the wake characteristics of a tidal stream turbine," Renewable Energy **132**, 989–997 (2019).

[50] P. Ouro and T. Stoesser, "Impact of environmental turbulence on the performance and loadings of a tidal stream turbine," Flow, Turbul. Combust. **102**, 613–639 (2019).

[51] A. Posa and R. Broglia, "Characterization of the turbulent wake of an axial-flow hydrokinetic turbine via large-eddy simulation," Comput. Fluids **216**, 104815 (2021).

[52] A. Posa and R. Broglia, "Momentum recovery downstream of an axial-flow hydrokinetic turbine," Renewable Energy **170**, 1275–1291 (2021).

[53] A. Posa, R. Broglia, and E. Balaras, "Recovery in the wake of in-line axial-flow rotors," Phys. Fluids **34**, 045104 (2022).

[54] F. Nicoud and F. Ducros, "Subgrid-scale stress modelling based on the square of the velocity gradient tensor," Flow, Turbul. Combust. **62**, 183–200 (1999).

[55] E. Balaras, "Modeling complex boundaries using an external force field on fixed Cartesian grids in large-eddy simulations," Comput. Fluids **33**, 375–404 (2004).

[56] J. Yang and E. Balaras, "An embedded-boundary formulation for large-eddy simulation of turbulent flows interacting with moving boundaries," J. Comput. Phys. **215**, 12–40 (2006).

[57] J. Yang, S. Preidikman, and E. Balaras, "A strongly coupled, embedded-boundary method for fluid-structure interactions of elastically mounted rigid bodies," J. Fluids Struct. **24**, 167–182 (2008).

[58] A. Posa, R. Broglia, and E. Balaras, "Instability of the tip vortices shed by an axial-flow turbine in uniform flow," J. Fluid Mech. **920**, A19 (2021).

[59] A. Posa, R. Broglia, and E. Balaras, "Flow over a hydrofoil in the wake of a propeller," Comput. Fluids **213**, 104714 (2020).

[60] A. Posa, R. Broglia, and E. Balaras, "The wake structure of a propeller operating upstream of a hydrofoil," J. Fluid Mech. **904**, A12 (2020).

[61] A. Posa, R. Broglia, and E. Balaras, "The wake flow downstream of a propeller-rudder system," Int. J. Heat Fluid Flow **87**, 108765 (2021).

[62] A. Posa, "Dependence of the wake recovery downstream of a vertical axis wind turbine on its dynamic solidity," J. Wind Eng. Ind. Aerodyn. **202**, 104212 (2020).

[63] A. Posa, "Influence of tip speed ratio on wake features of a vertical axis wind turbine," J. Wind Eng. Ind. Aerodyn. **197**, 104076 (2020).

[64] A. Posa, "Secondary flows in the wake of a vertical axis wind turbine of solidity 0.5 working at a tip speed ratio of 2.2," J. Wind Eng. Ind. Aerodyn. **213**, 104621 (2021).

[65] A. Posa, "Analysis of momentum recovery within the near wake of a cross-flow turbine using large Eddy simulation," Comput. Fluids **231**, 105178 (2021).

[66]K. Fukagata and N. Kasagi, "Highly energy-conservative finite difference method for the cylindrical coordinate system," J. Comput. Phys. **181**, 478–498 (2002).

[67]J. J. I. M. Van Kan, "A second-order accurate pressure-correction scheme for viscous incompressible flow," SIAM J. Sci. Statistical Comput. **7**, 870–891 (1986).

[68]T. Rossi and J. Toivanen, "Parallel fast direct solver for block tridiagonal systems with separable matrices of arbitrary dimension," SIAM J. Sci. Comput. **20**, 1778–1793 (1999).

[69]B. Gaurier, G. Germain, J. Facq, C. Johnstone, A. Grant, A. Day, E. Nixon, F. Di Felice, and M. Costanzo, "Tidal energy 'Round Robin' tests comparisons between towing tank and circulating tank results," Int. J. Mar. Energy **12**, 87–109 (2015).

[70]T. Lund, X. Wu, and K. Squires, "Generation of turbulent inflow data for spatially-developing boundary layer simulations," J. Comput. Phys. **140**, 233–258 (1998).

[71]R. Stevens, J. Graham, and C. Meneveau, "A concurrent precursor inflow method for large eddy simulations and applications to finite length wind farms," Renewable Energy **68**, 46–50 (2014).

[72]W. Munters, C. Meneveau, and J. Meyers, "Turbulent inflow precursor method with time-varying direction for large-eddy simulations and applications to wind farms," Boundary-Layer Meteorol. **159**, 305–328 (2016).

[73]T. Mukha and M. Liefvendahl, "The generation of turbulent inflow boundary conditions using precursor channel flow simulations," Comput. Fluids **156**, 21–33 (2017).

[74]P. Mycek, B. Gaurier, G. Germain, G. Pinon, and E. Rivoalen, "Experimental study of the turbulence intensity effects on marine current turbines behaviour. Part I: One single turbine," Renewable Energy **66**, 729–746 (2014).

[75]H. Quaranta, H. Bolnot, and T. Leweke, "Long-wave instability of a helical vortex," J. Fluid Mech. **780**, 687–716 (2015).

[76]H. Quaranta, M. Brynjell-Rahkola, T. Leweke, and D. Henningson, "Local and global pairing instabilities of two interlaced helical vortices," J. Fluid Mech. **863**, 927–955 (2019).

[77]L. Lignarolo, D. Ragni, C. Krishnaswami, Q. Chen, C. Simão Ferreira, and G. van Bussel, "Experimental analysis of the wake of a horizontal-axis wind-turbine model," Renewable Energy **70**, 31–46 (2014).

[78]L. Lignarolo, D. Ragni, F. Scarano, C. Simão Ferreira, and G. Van Bussel, "Tip-vortex instability and turbulent mixing in wind-turbine wakes," J. Fluid Mech. **781**, 467–493 (2015).

[79]A. Vinod and A. Banerjee, "Performance and near-wake characterization of a tidal current turbine in elevated levels of free stream turbulence," Appl. Energy **254**, 113639 (2019).

[80]M. Boudreau and G. Dumas, "Comparison of the wake recovery of the axial-flow and cross-flow turbine concepts," J. Wind Eng. Ind. Aerodyn. **165**, 137–152 (2017).

[81]M. Boudreau and G. Dumas, "Corrigendum to 'Comparison of the wake recovery of the axial-flow turbine and cross-flow turbine concepts' J of Wind Engineering and Industrial Aerodynamics (2017) 137–152," J. Wind Eng. Ind. Aerodyn. **177**, 155–156 (2018).

[82]P. Bachant and M. Wosnik, "Characterising the near-wake of a cross-flow turbine," J. Turbul. **16**, 392–410 (2015).

[83]P. Bachant and M. Wosnik, "Effects of Reynolds number on the energy conversion and near-wake dynamics of a high solidity vertical-axis cross-flow turbine," Energies **9**, 73–18 (2016).

[84]P. Bachant and M. Wosnik, "Modeling the near-wake of a vertical-axis cross-flow turbine with 2-D and 3-D RANS," J. Renewable Sustainable Energy **8**, 053311 (2016).

[85]P. Bachant, A. Goude, and M. Wosnik, "Actuator line modeling of vertical-axis turbines," arXiv:1605.01449 (2016).

[86]P. Ouro, S. Runge, Q. Luo, and T. Stoesser, "Three-dimensionality of the wake recovery behind a vertical axis turbine," Renewable Energy **133**, 1066–1077 (2019).

[87]S. Kang, Y. Kim, J. Lee, A. Khosronejad, and X. Yang, "Wake interactions of two horizontal axis tidal turbines in tandem," Ocean Eng. **254**, 111331 (2022).